NEUROSCIENCE

SHANK3 mutations disrupt olfactory valence coding across species, with cortical amygdala mechanisms identified in mice

Yu Hu[1,2]†, Yuli Wu[3]†, Mingyu Wei[4,5]†, Jingchao Ma[3,6], Jianbang Lin[1,6], Gaowei Chen[2], Qi Li[7], Jianqing Zhang[1], Ruiqi Wang[1], Yingjie Zhu[2], Qian Chen[6,8], Bo Peng[9], Yingying Zou[7], Bo Zhang[4,5]*, Wen Zhou[3,6]*, Zhonghua Lu[1,2,6,10]*

Mutations in *SHANK3* are a leading monogenic cause of autism spectrum disorder (ASD), often associated with profound sensory abnormalities. However, the impact of *SHANK3* deficiency on olfactory processing and the underlying neural mechanisms remains unclear. Here, we identify a cross-species disruption of olfactory valence perception in individuals with *SHANK3* mutations and in *Shank3* mutant mice. Patients carrying *SHANK3* mutations exhibited impaired valence-oriented sniffing and electroencephalography (EEG) responses, whereas *Shank3B*$^{-/-}$ mice displayed blunted behavioral responses to both attractive and aversive odors. In mice, these behavioral deficits were associated with attenuated odor-evoked calcium signals and reduced excitatory synaptic transmission in the cortical amygdala (CoA), a key node for olfactory valence processing. Acute CoA-specific Shank3 deletion recapitulated these deficits, whereas targeted restoration of CoA Shank3 expression rescued odor-induced appetitive and aversive behaviors. Our findings reveal a conserved function for *SHANK3* in encoding olfactory valence and identify CoA dysfunction as a circuit mechanism in mice.

INTRODUCTION

Loss-of-function mutations of the *SHANK3* gene are closely associated with Phelan-McDermid syndrome (PMS), a condition characterized by distinct autistic features (*1*). The *SHANK3* gene encodes a postsynaptic scaffold protein crucial for the development and function of glutamatergic synapses in various brain regions (*2*, *3*). Patients with *SHANK3* deficiency display a variety of clinical phenotypes, including intellectual disability, lack of language, developmental delay, and core autistic characteristics in social communication and stereotypic behaviors. Sensory deficits have recently been recognized as an important dimension of autistic symptoms and are incorporated into the diagnostic criteria for autism spectrum disorder (ASD) in DSM-5 (*4*). Patients with *SHANK3* deficiency exhibit hyporeactivity to multiple modalities of physical stimuli, including visual, tactile, and auditory stimuli (*5*). However, it remains unclear whether similar hyporeactivity toward chemical stimuli, especially olfactory cues that carry essential social and survival signals, exists in patients with *SHANK3* and which olfactory domains are affected.

The olfactory system detects environmental chemicals, driving both innate and adaptive behaviors, as well as physiological responses (*6*). Odorants and pheromones are detected by sensory neurons in the nose and relayed to the olfactory bulb (OB) and subsequently to the olfactory cortex, including the piriform cortex (PIR), the lateral entorhinal cortex (LENT), and the cortical amygdala (CoA) (*7*–*9*). Intact olfactory function is essential for foraging, reproduction, social communication, and general well-being (*10*–*12*). The primary dimension of olfactory perceptual space is valence (pleasantness), which is also one of the two dimensions that span emotional space and shape approach-avoidance responses (*13*–*15*). It is well documented in humans and rodents that the amygdala serves as a major hub in the encoding and representation of the valence values of odors and other sensory stimuli (*16*–*18*). The CoA, in particular, has been shown to underlie innate appetitive and aversive responses to odors (*19*). Moreover, abnormalities in emotional processing, including the processing of valence values, as well as in the structure and function of the amygdala, have also been associated with ASD (*20*–*24*).

In this study, we investigated spontaneous olfactory responses to odor valence both in children with *SHANK3* mutations and in *Shank3* mutant mice and explored the underlying neural circuitry mechanisms. We found that children with *SHANK3* mutations failed to differentiate between pleasant and unpleasant odors in terms of sniff parameters and EEG responses. Similarly, *Shank3* mutant mice showed deficits in olfactory valence processing of attractive and aversive odors. The latter was accompanied by altered neuronal activity and impaired synaptic transmission in the CoA. CoA-specific Shank3 knockout was sufficient to induce olfactory valence defects, whereas restoration of Shank3 in the CoA rescued olfactory valence-related behaviors in *Shank3* knockout mice. These results suggest a link between *SHANK3* deficiency and hyporeactivity to odor hedonics and identify an essential circuitry substrate for this chemosensory defect.

[1]Research Center for Primate Neuromodulation and Neuroimaging, Institute of Biomedical and Health Engineering, Shenzhen Institutes of Advanced Technology, Chinese Academy of Sciences, Shenzhen 518055, China. [2]Shenzhen-Hong Kong Institute of Brain Science, Shenzhen Institute of Advanced Technology, Chinese Academy of Sciences, Shenzhen 518055, China. [3]State Key Laboratory of Cognitive Science and Mental Health, Institute of Psychology, Chinese Academy of Sciences, Beijing 100101, China. [4]Institute of Neurological and Psychiatric Disorders, Shenzhen Bay Laboratory, Shenzhen 518132, China. [5]School of Chemical Biology and Biotechnology, Peking University Shenzhen Graduate School, Shenzhen 518055, China. [6]University of Chinese Academy of Sciences, Beijing 100049, China. [7]Department of Pathology and Pathophysiology, Faculty of Basic Medical Sciences, Kunming Medical University, Kunming 650500, China. [8]Zhongshan Institute for Drug Discovery, Shanghai Institute of Materia Medica, Chinese Academy of Sciences, Zhongshan 528400, China. [9]Institute for Translational Brain Research, Fudan University, Shanghai 200032, China. [10]State Key Laboratory of Biomedical Imaging Science and System, Chinese Academy of Sciences, Shenzhen 518055, China.
*Corresponding author. Email: zbo@pku.edu.cn (B.Z.); zhouwen@ucas.ac.cn (W.Z.); zh.lu@siat.ac.cn (Z.L.)
†These authors contributed equally to this work.

RESULTS

Aberrant sniffing and EEG responses to odor valence in children with *SHANK3* mutations

In light of the severe speech and cognitive deficits associated with *SHANK3* mutations (*25*, *26*), we leveraged variations in nasal flow during natural sniffing to conduct nonverbal assessments of odor valence discrimination in 21 children with *SHANK3* mutations (14 with terminal deletions of chromosome 22q13.3 encompassing the *SHANK3* gene, 3 with nonsense mutations, 3 with indels causing frameshift mutations, and 1 with a duplication; see table S1 for mutation details) and 42 age- and sex-matched typically developing (TD) controls. Pleasant (pineapple and chocolate) and unpleasant odors [trimethylamine (rotten fishlike odor) and isovaleric acid (sour stinky footlike odor)] were presented intermittently in random order while the children watched their favorite animation shows. Meanwhile, respirations were continuously measured using either a nasal cannula connected to a spirometer or a respiratory belt transducer (Fig. 1A). Each odor presentation lasted 7 s, typically encompassing two inhalations (odor sniffs).

Participants' sniff traces during odor presentations were normalized by the average durations and peak flowrates of the three inhalations preceding the odor presentation, accounting for odor-irrelevant fluctuations in respiration caused by the storylines of the animation shows. TD children exhibited stronger sniffs for pleasant odors compared to unpleasant ones, consistent with their odor valence ratings (fig. S1), whereas no such differentiation was observed in children with *SHANK3* (Fig. 1B). Instead, children with *SHANK3* displayed a general reduction in inhalation duration when exposed to odors (fig. S2), reflecting both their ability to detect odors and an overall avoidance of olfactory stimulation.

Further comparisons of the normalized mean sniff flowrate, peak sniff flowrate, and sniff volume during the presentations of pleasant versus unpleasant odors revealed that odor valence significantly modulated sniff vigor in TD children (mean sniff flowrate: $P = 5 \times 10^{-5}$, peak sniff flowrate: $P = 1.2 \times 10^{-5}$, and sniff volume: $P = 2.2 \times 10^{-4}$) but not in children with *SHANK3* (all *P*s > 0.5), with significant between-group differences across all three parameters (*P*s = 0.007, 0.002, and 0.006, respectively; Fig. 1, C to E). On the other hand, sniff duration and frequency remained unchanged between pleasant and unpleasant odors for both groups of children (TD: *P*s = 0.79 and 0.24; *SHANK3*: *P*s = 0.16 and 0.26; Fig. 1, F and G). These patterns persisted across both the first and second sniffs occurring during odor presentations (fig. S3). Moreover, in children with *SHANK3* mutations, the absence of valence modulation of sniff vigor was

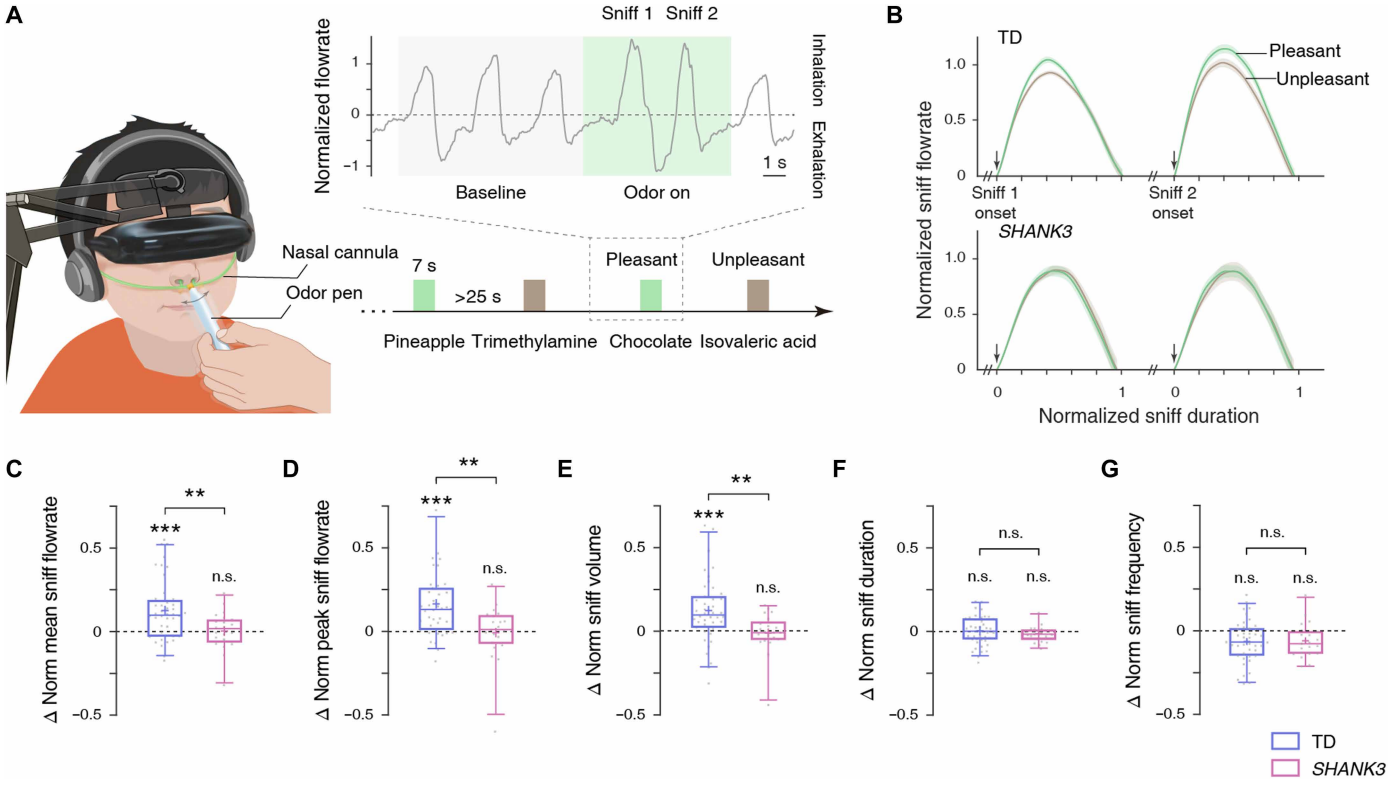

Fig. 1. Aberrant sniffing responses to pleasant and unpleasant odors in children carrying *SHANK3* mutations. (**A**) Experimental setup and procedure. Sniff 1 and Sniff 2 refer to the two inhalations that occurred during each 7-s presentation of an odor. (**B**) Averaged normalized sniff traces of Sniff 1 and Sniff 2 during the presentations of pleasant and unpleasant odors, respectively, in both TD ($n = 42$) and *SHANK3* ($n = 21$) children. On the vertical axis, 0 represents no flowrate (sniff onset), whereas 1 denotes the baseline peak inhalation flowrate. Shaded areas: SEMs. (**C** to **G**) Differences between sniff response to pleasant and unpleasant odors in terms of normalized mean sniff flowrate (C), peak sniff flowrate (D), sniff volume (E), sniff duration (F), and sniff frequency (G) in both TD children and children with *SHANK3*. Significant modulations by odor valence were found among TD children for normalized mean sniff flowrate, peak sniff flowrate, and sniff volume but not among children with *SHANK3*, with significant between-group differences in all of these parameters. Sniff duration and frequency were not significantly affected by odor valence in both groups of children. In each box and whisker plot, the middle line denotes the medium, the cross denotes the mean, the bottom and top edges of the box indicate the 25th and 75th percentiles, respectively, and the ends of the whiskers represent the 5th and 95th percentiles. Dots represent individual children. $^{**}P < 0.01$; $^{***}P < 0.001$; n.s., not significant.

evident both in those with additional gene deletions (*SHANK3*+, $n = 13$) and in those with *SHANK3* mutations alone (*SHANK3* only, $n = 8$) (fig. S4).

We also obtained usable scalp electroencephalography (EEG) recordings from an additional seven children with *SHANK3* mutations and seven age- and sex-matched TD children. Using a modified testing procedure (fig. S5A), olfactory stimuli were presented intermittently and in random order via a computer-controlled olfactometer while the children watched their preferred animation shows. The stimuli included pineapple (pleasant) and trimethylamine (unpleasant) at clearly noticeable concentrations (1×), the same odors at 1/10 of those concentrations (0.1×), and purified air as a control. Each stimulus was delivered for 3 s with an interstimulus interval of ~18 s. During each olfactory stimulus presentation, the ongoing animation was replaced by a fixed frame (without audio) to facilitate EEG comparisons across olfactory conditions. EEG signals were aligned to sniff onsets during periods of olfactory stimulation.

Corroborating the results obtained with sniff parameters, time-frequency analysis of EEG signals in TD children revealed a significant differentiation of odor valence at Pz—the electrode strongly implicated in olfactory processing (*27*, *28*)—in alpha-band power around 700 to 800 ms following inhalation onset ($P = 0.007$; fig. S5B). This observation aligns with earlier olfactory EEG findings in healthy adults (*29*–*31*). In contrast, no significant valence-related effect was observed in children with *SHANK3* mutations ($P = 0.13$, $BF_{10} = 0.98$, and error% = 0.0198; fig. S5B). The absence of valence differentiation was not attributable to general olfactory hyposensitivity. Compared with purified air, odors (pineapple and trimethylamine combined) at clearly perceptible concentrations elicited significant theta-alpha activity around 500 ms following inhalation onset in both TD children and children with *SHANK3* (TD: $P = 0.011$; *SHANK3*: $P = 0.016$), with no group differences in event-related percent change in power (ER%) ($P = 0.49$, $BF_{10} = 0.53$, and error% = 0.00107; fig. S5C). At 0.1× concentration, these odors produced similar, although weaker (TD: $P = 0.028$; *SHANK3*: $P = 0.028$) and non-significant, time-frequency responses in both groups (TD versus *SHANK3*, $P = 0.50$, $BF_{10} = 0.52$, and error% = 0.00105; fig. S5C). In other words, children with *SHANK3* exhibited EEG responses, indicating sensitivity to odors and odor gradients comparable to those of TD children.

Together, these observations highlight hyporeactivity to odor hedonics—but not to odors per se—in children with *SHANK3* mutations, suggesting a potential link between *SHANK3* deficiency and olfactory anhedonia.

Aberrant behavioral responses to odor valence in *Shank3* mutant mice

Given the observation of olfactory valence processing deficits in children with *SHANK3* mutations, we used *Shank3B*$^{-/-}$mice—harboring a comparable loss-of-function mutation—to investigate whether this phenotype is conserved in rodent models. Using a refined performance index (PI) to quantify odor-evoked valence responses (*19*), we observed pronounced differences between wild-type (WT) and *Shank3B*$^{-/-}$ mice (KO). WT mice displayed strong aversion to negatively valenced odorants such as 2,5-dihydro-2,4,5-trim ethylthiazoline (TMT) and pentanal and robust attraction to positively valenced odorants including isoamyl acetate (IAA) and 2-phenylethanol (2-PE) (Fig. 2A). In contrast, *Shank3B*$^{-/-}$ mice showed markedly blunted aversion to TMT and pentanal, as well as reduced—or in some cases reversed—attraction to appetitive odorants strongly preferred by WT mice. These alterations indicate that *Shank3* deficiency disrupts the normal coding of both attractive and aversive odor valence. On the basis of these results, we selected 2-PE and TMT as representative appetitive and aversive odorants, respectively, for subsequent mechanistic experiments (*32*).

TMT application elicited robust defensive responses in WT mice, characterized by rapid escape (reflected by increased maximum velocity) followed by prolonged freezing. In contrast, *Shank3B*$^{-/-}$ mice failed to show either flight or freezing in response to TMT (Fig. 2, D and E, WT versus KO mice, in D: $P = 0.359$ in water, $P = 0.907$ in 2-PE, and $P = 0.008$ in TMT; in E: $P = 0.562$ in water, $P = 0.884$ in 2-PE, and $P < 0.001$ in TMT) and instead spent significantly more time investigating the TMT source (Fig. 2C). *Shank3B*$^{-/-}$ mice also exhibited a marked reduction in attraction to 2-PE (Fig. 2C, WT versus KO mice, $P = 0.479$ in water, $P = 0.001$ in 2-PE, and $P = 0.002$ in TMT). Apart from the TMT-evoked changes in maximum velocity and immobility, the total distance traveled did not differed between groups (Fig. 2F), indicating that the behavioral alterations in *Shank3B*$^{-/-}$ mice reflect selective impairments in odor-evoked valence processing rather than generalized motor deficits. Therefore, consistent with children carrying the *SHANK3* mutations, *Shank3B*$^{-/-}$ mice failed to engage in normal responses toward odors with distinct valence.

To investigate whether the abnormal response observed during the presentation of attractive and aversive odorants in *Shank3B*$^{-/-}$ mice was a result of the inability to differentiate between odors, we trained mice to associate a set of odors with differential outcomes (fig. S6A). Each training trial began with a conditioned stimulus (CS) of an odor, followed by a 2-s delay (the response window) and then an unconditioned stimulus (US; water, nothing, or air puff) (fig. S6, B and C). As training progressed, both WT and *Shank3B* $^{-/-}$ mice exhibited anticipatory licks only during the delay before water trials, indicating the establishment of an odor-based CS-US association (fig. S6, D and F). In this associative learning paradigm, there was no significant difference between WT and *Shank3B*$^{-/-}$ mice (fig. S6E), suggesting that *Shank3B*$^{-/-}$ mice are capable of perceiving and discriminating between different odorants, as evidenced by their ability to form odor-specific conditioned responses in a classical associative learning task.

Mutant *Shank3B*$^{-/-}$ mice have reduced neuronal activation in the CoA

Next, we sought to identify the neural circuit substrate that was affected by the loss of Shank3 and that played key roles in the observed valence coding defects in *Shank3B*$^{-/-}$ mice. Because a previous study indicated that the CoA is essential for behavioral responses toward appetitive and aversive odors (*19*), we asked whether the activity of the CoA was abnormal in *Shank3* mutant mice. Immunohistochemical analysis of the immediate early gene product c-Fos revealed a robust elevation of the number of c-Fos$^+$ neurons in the OB, the CoA, and the PIR after 2-PE and TMT stimulation in WT mice when contrasted with the *Shank3* group. However, c-Fos induction was significantly lower in the CoA of *Shank3B*$^{-/-}$ mice compared to WT mice, indicating attenuation of c-Fos in the *Shank3* group ($P = 0.523$ in water, $P = 0.006$ in 2-PE, and $P < 0.001$ in TMT). In contrast, there were no significant between-group differences in the number of c-Fos$^+$ neurons in the OB or PIR (Fig. 3, A and B).

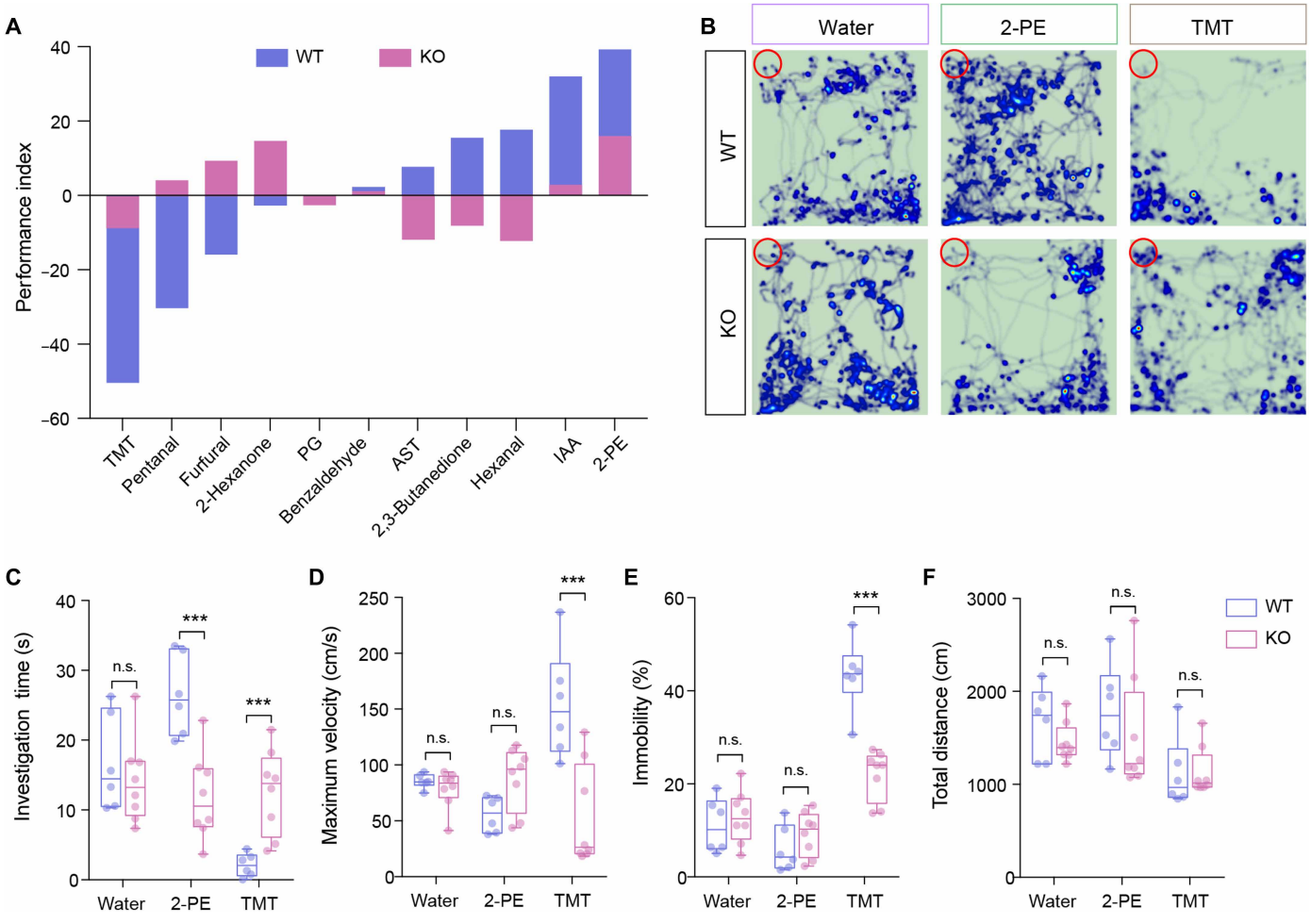

Fig. 2. Aberrant behavioral responses suggesting impaired odor valence detection. (**A**) The average response to an array of odorants is quantified by a PI in WT and *Shank3B*$^{-/-}$ (KO) mice. (**B**) Representative heatmaps of animal movement for odor-driven behavior. The orange circles in the corner represent papers with water, 2-PE, or TMT, respectively. (**C** to **F**) Quantifications of investigation time spent in the circled area containing the odor (C), maximum velocity in targeted arena (D), percentage of immobility time (E), and total distance (F) during odor exposure in WT and KO mice. For each box and whisker plot, the middle line denotes the median, the bottom and top edges of the box indicate the 25th and 75th percentiles, respectively, and the ends of the whiskers represent the minimum and maximum percentiles. Dots represent individual mice. ***$P < 0.001$; n.s., not significant.

We then recorded real-time calcium signals of CoA and PIR neurons in head-fixed mice during 2-PE and TMT stimulations after intracranial delivery of AAV9-*CaMKIIα-GCaMP6s* into these brain regions (Fig. 3, C to E), which enables selective labeling of excitatory neurons (*33*). We observed a strong transient increase in GCaMP fluorescence in WT mice elicited by 2-PE and TMT. In contrast, there was only a mild increase in genetically encoded calcium indicator GCaMP (comprising GFP, calmodulin, and the M13 peptide) fluorescence in *Shank3B*$^{-/-}$ mice (Fig. 3F). The normalized GCaMP fluorescence change ($\Delta F/F$) during 2-PE and TMT stimulations was significantly lower in *Shank3B*$^{-/-}$ mice compared to that in WT mice (Fig. 3H, $P = 0.009$ in 2-PE and $P = 0.029$ in TMT). Unlike in the CoA, we did not observe a significant difference in calcium responses in the PIR (Fig. 3, G and I). These data suggest that reduced activation of CoA excitatory neurons may contribute to the olfactory valence deficit in *Shank3B*$^{-/-}$ mice.

Dysfunctional synaptic transmission of CoA pyramidal neurons in *Shank3B* $^{-/-}$ mice

Diminished activation of CoA excitatory neurons may underlie the olfactory valence deficit observed in *Shank3B*$^{-/-}$ mice. To investigate the potential impact of Shank3 loss on synaptic functions in the CoA, we conducted whole-cell patch-clamp recording on pyramidal neurons in Layer I of the CoA, where axons from the OB projection neurons terminate. We recorded the miniature excitatory postsynaptic currents (mEPSCs) after blocking sodium channels with QX314 in the pipette solution and action potentials and inhibitory synaptic transmission with tetrodotoxin (TTX) and picrotoxin in the perfusion solution. We found that both mEPSC frequency and amplitude were significantly reduced in *Shank3B*$^{-/-}$ mice compared with those littermate control mice (Fig. 4, A to C), suggesting a weaker excitatory synaptic strength in *Shank3B*$^{-/-}$ mice. To directly measure the synaptic strength of OB-CoA synapses, we selectively stimulated

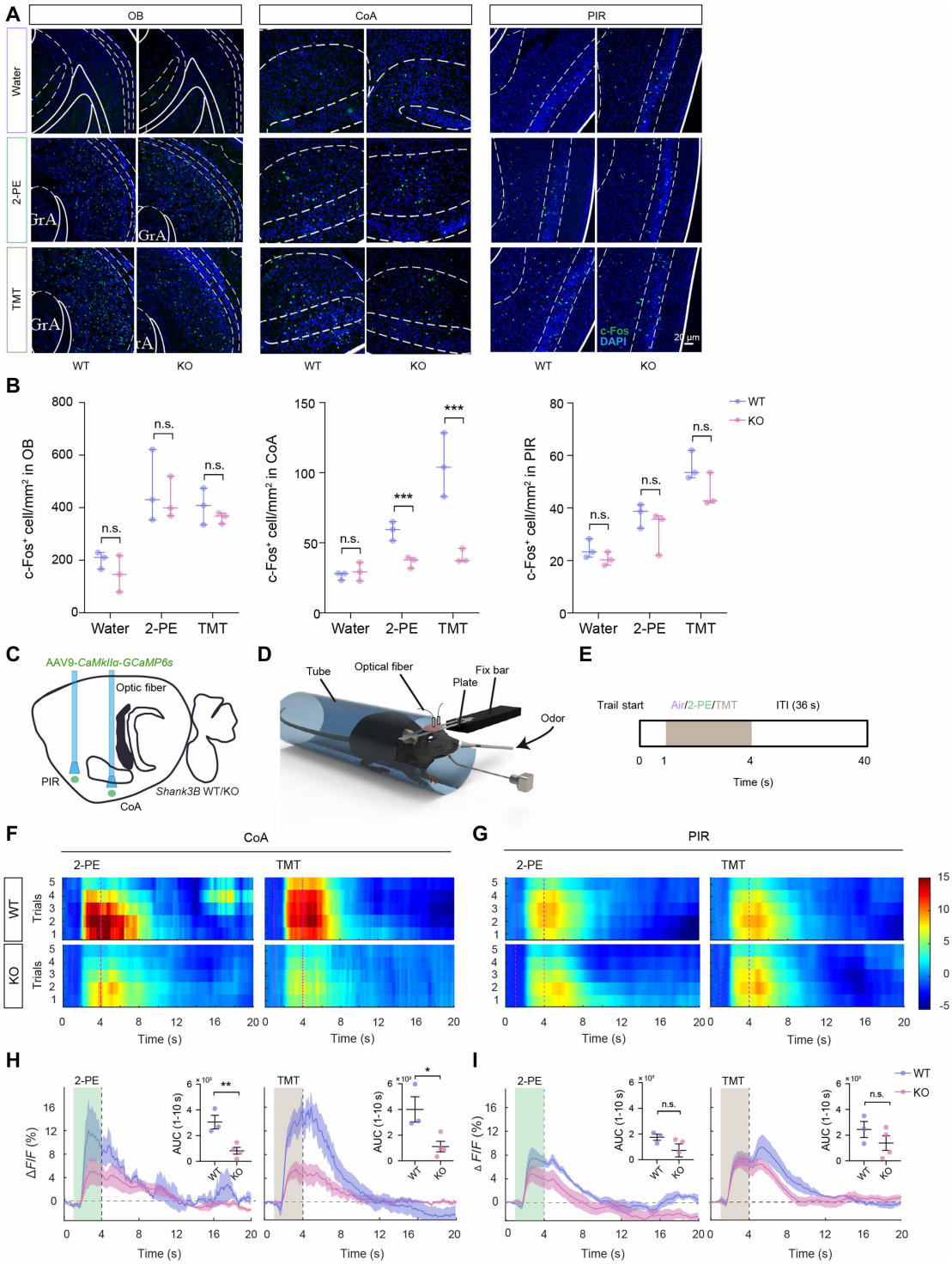

Fig. 3. Selective reduced neuronal activity in the CoA, but not in the PIR, in *Shank3B*$^{-/-}$ mice. (**A**) Representative images of c-Fos^{+} cells in the OB, CoA, and PIR cortex in WT and *Shank3B*$^{-/-}$ mice. Scale bar, 20 μm. (**B**) Quantification of c-Fos^{+} cells in the OB (left), CoA (middle), and PIR cortex (right) from each group of animals. (**C**) Schematic showing the experimental setup used to record calcium signaling activity in GCaMP6-expressing neurons using fiber photometry in WT and *Shank3B*$^{-/-}$ (KO) mice. (**D** and **E**) Schematic showing the optical fiber placement and trial sequence. ITI, intertrial interval. (**F** and **G**) Heatmaps illustrating the calcium response (Δ*F*/*F*, %) of CoA and PIR cortex neurons during 2-PE and TMT stimulation. (**H** and **I**) Mean GCaMP response curves and area under each curve. Box and whisker plots are as in Fig. 2. Error bars, SEM. Dots represent individual mice. **P* < 0.05; ***P* < 0.01; ****P* < 0.001; n.s., not significant.

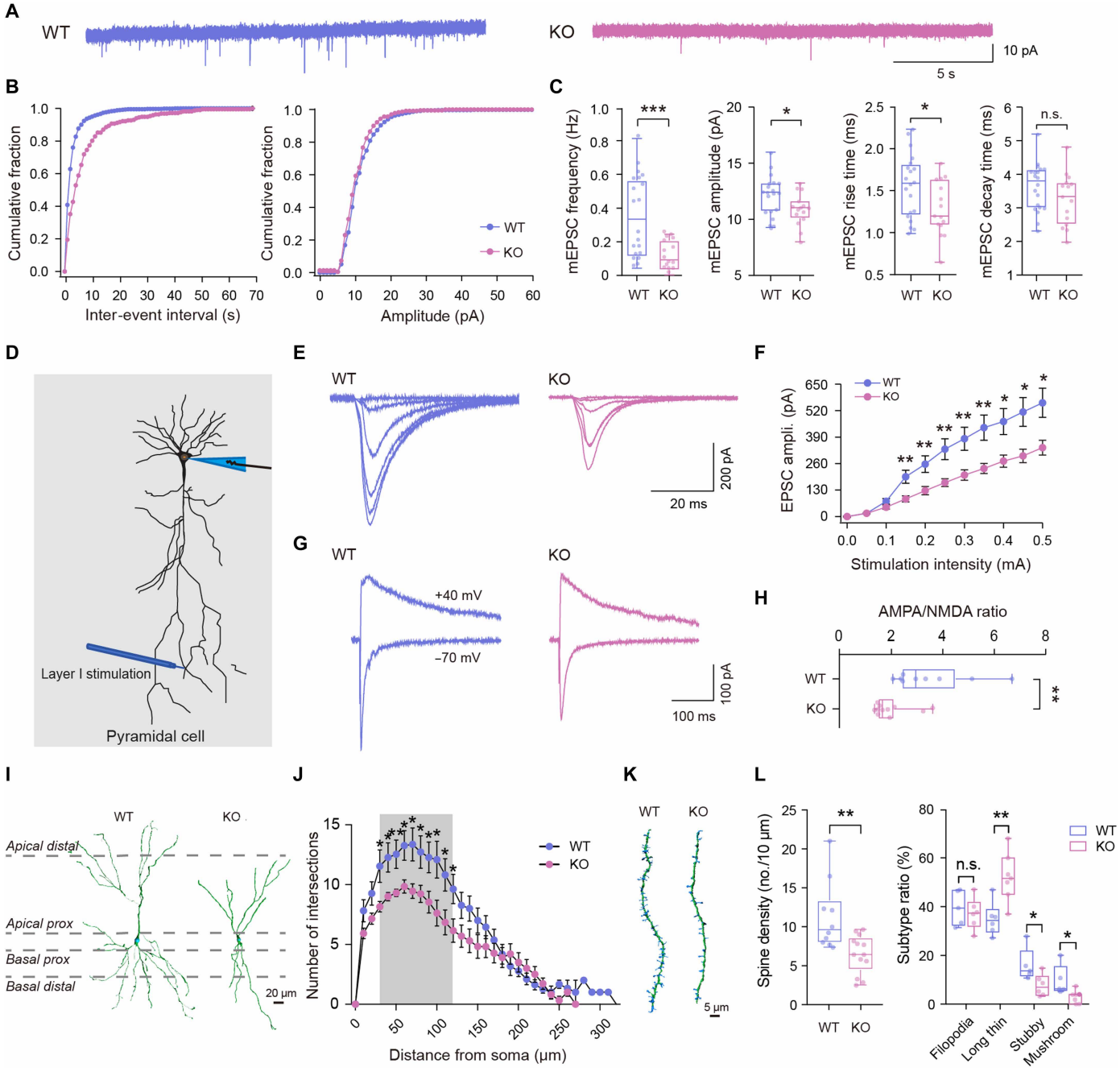

Fig. 4. Dysfunctional synaptic transmission in the CoA of *Shank3B*$^{-/-}$ mice. (**A**) Representative mEPSC traces in CoA pyramidal neurons in WT and *Shank3B*$^{-/-}$ (KO) mice. (**B** and **C**) Summary data for mEPSC cumulative plots, frequency, amplitude, rise time, and decay time in CoA pyramidal neurons obtained from WT and KO mice. (**D**) Schematic showing the experimental setup. (**E**) Representative traces of AMPAR-mediated evoked EPSCs in CoA pyramidal neurons obtained from Layer I of WT and KO mice. (**F**) Summary data for the peak amplitudes of evoked AMPAR-EPSCs in response to different levels of stimulation intensity. (**G**) Representative trace of AMPA-to-NMDA EPSC ratio from Layer I of *Shank3B* WT and KO mice. (**H**) Summary data for the AMPA-to-NMDA EPSC ratio from Layer I of CoA pyramidal neurons in *Shank3B* WT and KO mice. (**I**) Representative dendrite processes and reconstructed images from the CoA of WT and KO mice. Scale bar, 20 μm. (**J**) Sholl analysis showing the dendritic complexity of CoA in KO mice compared to WT mice. (**K**) Representative spines and reconstructed images from Layer I of the CoA in *Shank3B* WT (left) and KO mice (right). Scale bar, 5 μm. (**L**) Total dendritic spine density and the classification of subtype spines in the Layer I of the CoA in *Shank3B* WT and KO mice. For bar charts, bars depict the mean and error bars represent the SEM. Box and whisker plots are as in Fig. 2. **P* < 0.05; ***P* < 0.01; ****P* < 0.001; n.s., not significant.

OB-CoA synapses by positioning the stimulating electrodes in CoA Layer I and recorded the evoked AMPA receptor (AMPAR)–mediated EPSCs from CoA pyramidal neurons in response to stimuli of different intensities (Fig. 4D). We found that the amplitude of EPSCs was significantly lower in *Shank3B*$^{-/-}$ mice (Fig. 4, E and F). Consistent with the smaller AMPAR-mediated EPSCs, a lower AMPA-to-NMDA (*N*-methyl-D-aspartate) ratio was observed in *Shank3B*$^{-/-}$ mice (Fig. 4, G and H). To assess whether this synaptic alteration was region specific, mEPSC recordings from pyramidal neurons in the PIR showed no significant differences in frequency, amplitude, rise time, or decay time between WT and *Shank3B*$^{-/-}$ mice (fig. S7, A to C). Together with these findings, the lower frequency of mEPSCs observed in the CoA of *Shank3B*$^{-/-}$ mice implies a potential contribution of presynaptic deficit. To exclude this possibility, we measured the presynaptic release probability by assessing the paired-pulse ratio (PPR) of EPSCs, and we found no differences in the PPR between genotypes (fig. S7, D and E). These results demonstrate that excitatory synaptic transmission of OB-CoA synapses was impaired in *Shank3B*$^{-/-}$ mice and that this deficit is unlikely to be caused by altered presynaptic release probability.

Dendritic and spine morphology of CoA pyramidal neurons in *Shank3B*$^{-/-}$ mice are abnormal

Given that Shank3 plays a critical role in both synapse formation and function (*3*), we sought to determine whether the *Shank3* deletion would induce structural changes in the pyramidal neurons of the CoA. To examine the dendritic processes and spines of CoA pyramidal neurons, we made local injections of a mixture of AAV9-*CaMKII*α-*Cre* (1:10,000) and AAV9-*EF1*α-*DIO-EGFP* to sparsely label neurons with green fluorescent protein (GFP) in WT and *Shank3B*$^{-/-}$ mice. We then analyzed the dendritic processes and spines of pyramidal neurons in Layer I of the CoA where they receive olfactory inputs from the OB. The Sholl analysis indicated that the dendritic complexity of CoA pyramidal neurons in *Shank3B*$^{-/-}$ mice was lower compared to that of WT mice (Fig. 4, I and J). We also found a decrease in the number of intersections between 30 and 120 μm away from the soma in *Shank3B*$^{-/-}$ mice. Significantly lower total dendritic spine density was also observed in *Shank3B*$^{-/-}$ mice. We further classified different types of spines. Among the different spine types, the ratios of mushroom and stubby were reduced, whereas long thin spines increased, and filopodia spines remained unaltered in Layer I of the CoA in *Shank3B*$^{-/-}$ mice (Fig. 4, K and L). These observations demonstrated dendritic and spine morphology abnormalities consistent with synaptic function defects caused by the loss of Shank3.

Selective deletion of Shank3 in the CoA induces odor valence perception deficits

To establish a causal link between the loss of Shank3 in CoA neurons and defective odor valence–driven behaviors, we used a targeted strategy to selectively knock out Shank3 expression in the CoA of adult C57BL/6J mice using CRISPR-Cas9 technology. We bilaterally injected AAV9-*pCALM1-SpCas9-miniU6-sgRNA*^{Shank3} into the CoA to generate an acute *Shank3* knockout model (Fig. 5, A and B, and fig. S8). Consistent with observations in *Shank3B*$^{-/-}$ mice, acute ablation of Shank3 in CoA neurons led to a decrease in the frequency of mEPSCs (Fig. 5, C to E), whereas the presynaptic release probability, as assessed by PPR, remained intact (fig. S9, A and B). Using the AAV-*SpCas9-sgRNA* system, we achieved a highly specific knockdown of Shank3 in the CoA, with *Shank3* mRNA levels reduced to 41.5% ± 6.3% of control levels (fig. S8B) and a corresponding loss of Shank3 protein (46.0% ± 4.7%; fig. S8, C and D), with no detectable changes in the adjacent PIR. These results demonstrate that the CRISPR-Cas9 manipulation efficiently and selectively disrupts Shank3 expression within the CoA while sparing surrounding olfactory cortical regions (fig. S8, B to D).

Furthermore, the amplitude of evoked AMPAR-mediated EPSCs in response to stimuli at 0.4 and 0.5 mA was reduced, indicating impaired postsynaptic responsiveness. Assessment of attraction and aversion responses with 2-PE and TMT revealed dysfunctional odor valence assessment in acute CoA Shank3 knockout mice, as evidenced by reduced and increased investigation time toward 2-PE and TMT, respectively (Fig. 5G, *sgRNA*^{Scr} versus *sgRNA*^{Shank3} mice, $P = 0.459$ in water, $P = 0.007$ in 2-PE, and $P < 0.001$ in TMT). Consistent with their altered valence response, *sgRNA*^{Shank3} mice showed significantly attenuated the maximum velocity and reduced immobility in response to TMT compared to mice injected with the control AAV expressing a scrambled (Scr) single guide RNA (sgRNA) (Fig. 5, H and I, *sgRNA*^{Scr} versus *sgRNA*^{Shank3} mice; in H: $P = 0.996$ in water, $P = 0.728$ in 2-PE, and $P < 0.001$ in TMT; in I: $P = 0.285$ in water, $P = 0.841$ in 2-PE, and $P < 0.001$ in TMT). Furthermore, compared with *sgRNA*^{Scr} mice, *Shank3* acute ablation mice exhibited lower calcium signals in the CoA during 2-PE and TMT stimulations (Fig. 5, K and L, $P = 0.015$ in 2-PE and $P = 0.002$ in TMT). Collectively, these findings demonstrate that acute loss of Shank3 specifically within the CoA was sufficient to damage odor valence perception.

Restoration of Shank3 expression in the CoA rescues odor valence responses in *Shank3* knockout mice

To further determine whether the loss of Shank3 in the CoA is essential to odor valence–induced behavioral abnormalities in *Shank3* knockout mice, we selectively restored Shank3 expression in the CoA. We used a *Shank3* conditional knock-in (CKI) mouse model where Shank3 expression can be reinstated upon Cre recombinase expression in a *Shank3* knockout background (*34*). In the *Shank3* CKI mouse model, exons 13 to 16 encoding the PDZ domain are inverted and transcriptionally silenced using the FLEx switch. Delivery of AAV-*Cre* into the CoA induces Cre-dependent recombination, restoring the correct orientation of the inverted exon cassette. This recombination reinstates endogenous Shank3 expression specifically in CoA neurons that receive Cre, thereby enabling region-specific rescue of Shank3 function (Fig. 6A). Similar to *Shank3B*$^{-/-}$ mice, *Shank3* CKI mice displayed defective behavioral responses toward 2-PE and TMT (fig. S10). We then injected AAV8-*CaMKII*α-*Cre-EYFP* into the CoA of *Shank3* CKI mice to restore the reexpression of most Shank3 isoforms in the CoA but not in the PIR (Fig. 6, A to C, and fig. S11). In electrophysiological analyses, we found that reduced mEPSC frequency in *Shank3* CKI mice was effectively restored after Cre expression (Fig. 6, D to F). The impaired synaptic strength of OB-CoA synapses was also reversed (Fig. 6G), whereas the presynaptic release probability was intact after the restoration of Shank3 expression (fig. S12, A and B).

We then injected a mixture of AAV9-*CaMKII*α-*FLP* (1:10,000) and AAV9-*EF1*α-*fDIO- mCherry* into *Shank3* CKI mice to sparsely label pyramidal neurons in Layer I of the CoA and analyzed the

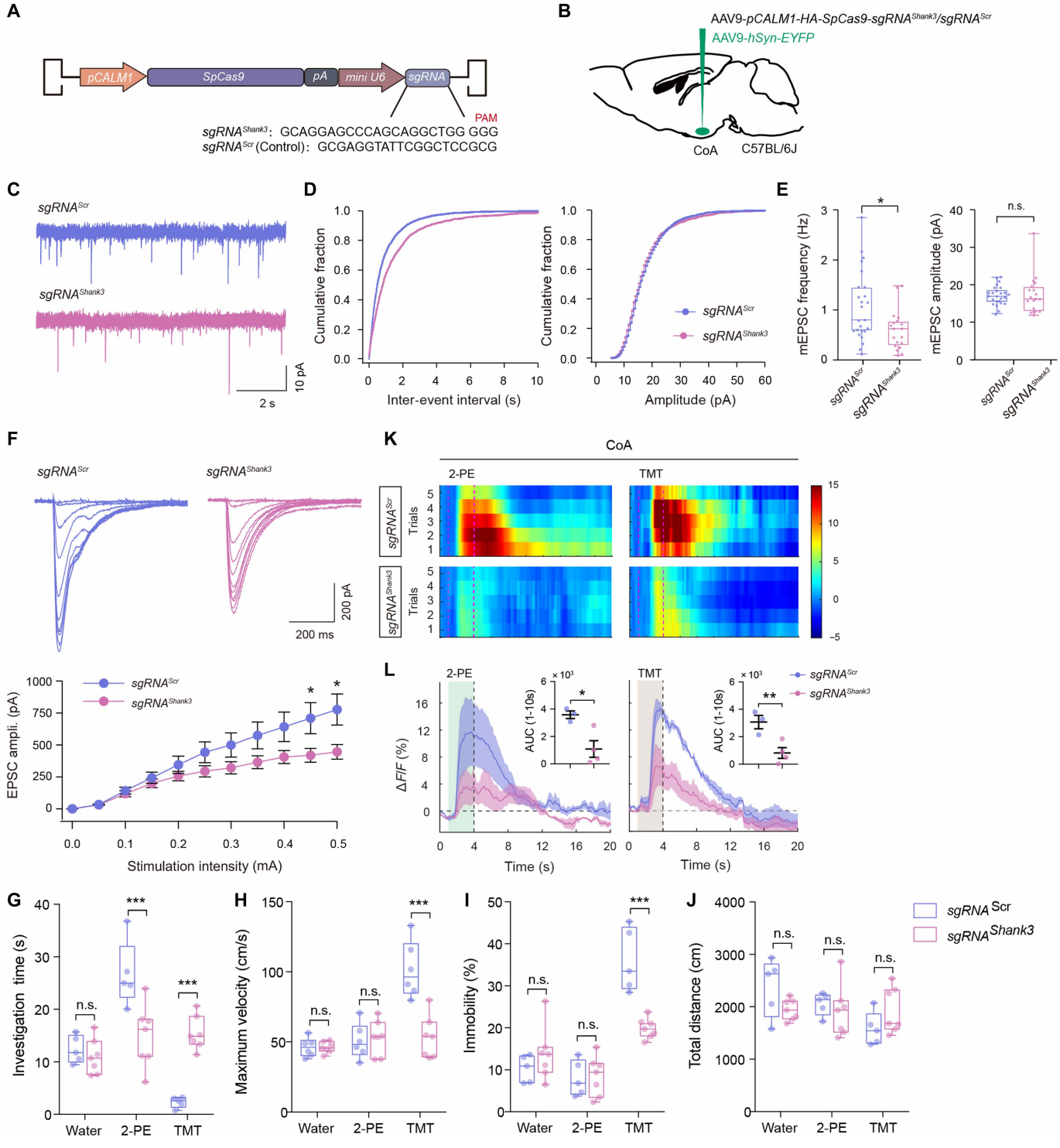

Fig. 5. Acute deletion of *Shank3* in the CoA induced valence detection deficits in mice. (**A** and **B**) Strategy for specific deletion of *Shank3* using AAV9-*pCALM1-SpCas9-miniU6-sgRNA*^{Shank3} and using AAV9-*pCALM1-SpCas9-miniU6-sgRNA*^{Scr} as a control. (**C**) Representative mEPSC traces in CoA pyramidal neurons in *sgRNA*^{Scr} and *sgRNA*^{Shank3} mice. (**D** and **E**) Summary data for mEPSC cumulative plots, frequency, and amplitude in CoA pyramidal neurons obtained from *sgRNA*^{Scr} and *sgRNA*^{Shank3} mice. (**F**) Representative traces of AMPAR-mediated evoked EPSCs in CoA pyramidal neurons obtained from *sgRNA*^{Scr} and *sgRNA*^{Shank3} mice (top) and summary data for the peak amplitudes of evoked AMPAR-EPSCs in response to different stimulation intensities. (**G** to **J**) Quantification of investigation time in the stimulation circle (G), maximum velocity in targeted arena (H), percentage of immobility time (I), and total distance traveled (J) during odor exposure in *sgRNA*^{Scr} and *sgRNA*^{Shank3} mice. (**K**) Heatmaps illustrating the calcium response (Δ*F*/*F*, %) of CoA neurons during TMT and 2-PE stimulation in *sgRNA*^{Scr} and *sgRNA*^{Shank3} mice. (**L**) Mean GCaMP response curves and area under each curve. Box and whisker plots are as in Fig. 2. Error bars, SEM. Dots represent individual mice. **P* < 0.05; ***P* < 0.01; ****P* < 0.001; n.s., not significant.

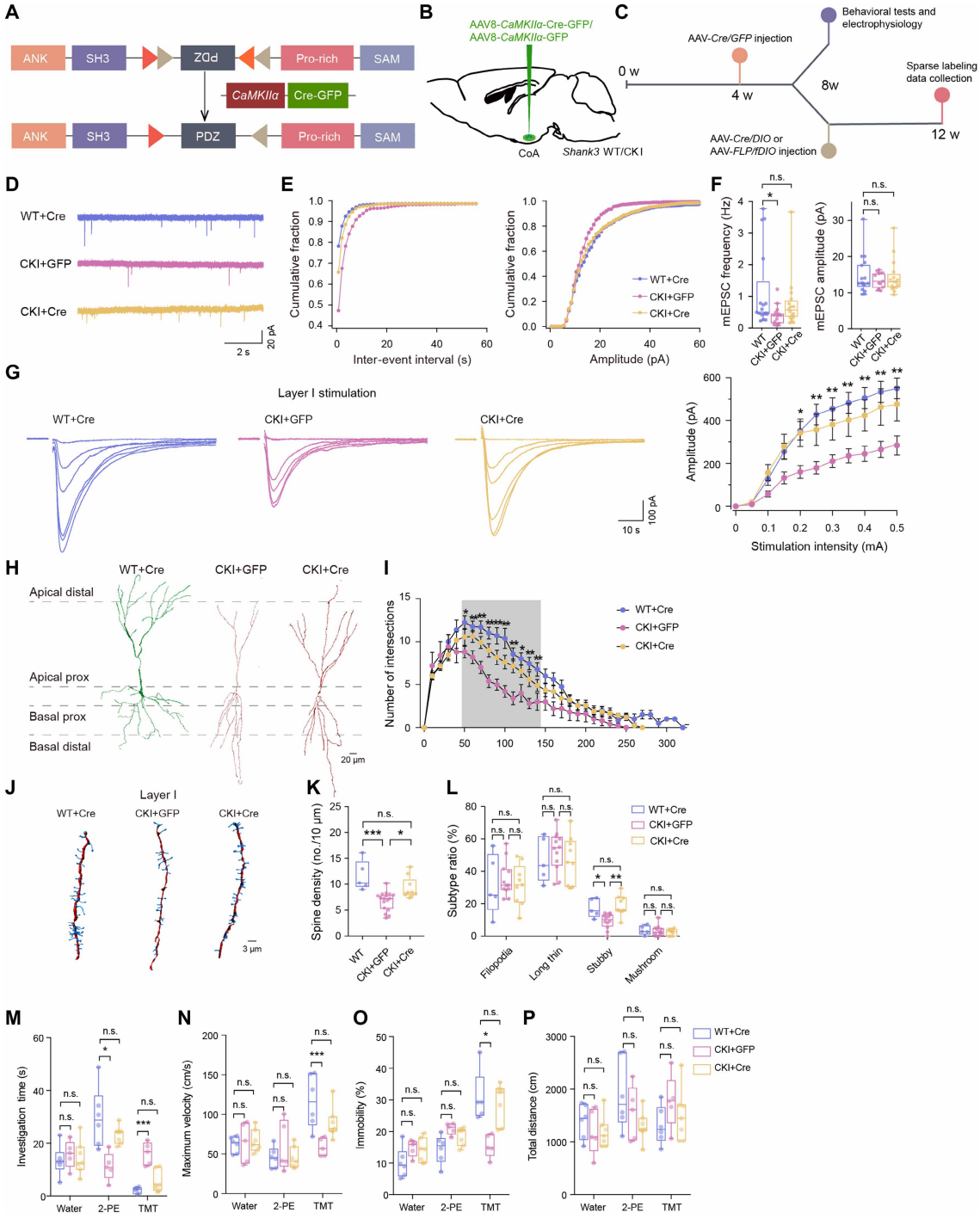

Fig. 6. Targeted restoration of Shank3 expression in the CoA of *Shank3* CKI mice rescued odor valence detection abnormalities. (**A**) Strategy to explore the effects of adult reexpression of Shank3 using a *Shank3* CKI mouse model. (**B** and **C**) Schematic diagram and the representative image showing stereotaxic injections of AAV8-*CaMKIIα-Cre-GFP* and AAV8-*CaMKIIα-GFP* into the CoA of WT and CKI mice. w, weeks. (**D**) Representative mEPSC traces in CoA pyramidal neurons in *Shank3* WT + Cre, CKI + GFP, and CKI + Cre mice. (**E** and **F**) Summary data for mEPSC cumulative plots, frequency, amplitude, rise time, and decay time in CoA pyramidal neurons obtained from all three groups of mice. (**G**) Representative traces of AMPAR-mediated evoked EPSCs in CoA pyramidal neurons from each of the three mouse groups (left) and summary data for the peak amplitudes of evoked AMPAR-EPSCs in response to different levels of stimulation intensity. (**H**) Representative spines and reconstructed images in Layer I of the CoA in *Shank3* WT, CKI + GFP, and CKI + Cre mice. Scale bar, 20 μm. (**I**) Sholl analysis showing the dendritic complexity in the CoA from all three mouse groups. (**J**) Representative dendrites process and reconstructed images in the CoA of *Shank3* WT, CKI + GFP, and CKI + Cre mice. Scale bar, 3 μm. (**K**) Total dendritic spine density in Layer I of the CoA in all three groups. (**L**) Classification of subtype spines of the CoA in all three groups. (**M** to **P**) Quantification of investigation time in the stimulation circle (M), maximum velocity in targeted arena (N), percentage of immobility time (O), and total distance traveled (P) during odor exposure in *Shank3* WT, CKI + GFP, and CKI + Cre mice. Box and whisker plots are as in Fig. 2. Error bars, SEM. **P* < 0.05; ***P* < 0.01; ****P* < 0.001; n.s., not significant.

anatomical features of dendritic processes after Shank3 restoration. We found elevated number of intersections and spines in the Layer I portion of CoA pyramidal neurons after reinstating Shank3 expression in *Shank3* CKI mice (Fig. 6, H to L). Intriguingly, reexpression of Shank3 in the CoA alone was sufficient to rescue attraction and avoidance elicited by 2-PE and TMT in *Shank3* CKI mice, respectively [Fig. 6, M to O; one-way analysis of variance (ANOVA) followed by Dunnett's test; in M: CKI + GFP versus WT + Cre, $P = 0.721$; CKI + Cre versus WT + Cre, $P = 0.916$, in water; CKI + GFP versus WT + Cre, $P = 0.002$; CKI + Cre versus WT + Cre, $P = 0.222$, in the 2-PE group; CKI + GFP versus WT + Cre, $P < 0.001$; CKI + Cre versus WT + Cre, $P = 0.206$, in TMT; in N: CKI + GFP versus WT + Cre, $P = 0.957$; CKI + Cre versus WT + Cre, $P = 0.858$, in water; CKI + GFP versus WT + Cre, $P = 0.435$; CKI + Cre versus WT + Cre, $P = 0.997$, in the 2-PE group; CKI + GFP versus WT + Cre, $P = 0.002$; CKI + Cre versus WT + Cre, $P = 0.102$, in TMT; in O: CKI + GFP versus WT + Cre, $P = 0.114$; CKI + Cre versus WT + Cre, $P = 0.161$, in water; CKI + GFP versus WT + Cre, $P = 0.852$; CKI + Cre versus WT + Cre, $P = 0.097$, in the 2-PE group; CKI + GFP versus WT + Cre, $P = 0.040$; CKI + Cre versus WT + Cre, $P = 0.867$, in TMT]. These data strongly argue that Shank3 expression in the CoA is essential to the intact olfactory valence coding in mice.

DISCUSSION

Across the animal kingdom, volatile chemicals serve as signals that elicit immediate approach or avoidance behaviors—emotional responses integral to social functioning (*35*, *36*). Our findings reveal significant deficits in odor valence processing in both children with *SHANK3* mutations and *Shank3B* mutant mice. Neurophysiological examinations of *Shank3B* mutant mice identified reduced neuronal activity, aberrant synaptic transmission, and altered dendritic and spine morphology within the CoA. Critically, targeted deletion of *Shank3* in CoA neurons impaired odor valence processing, whereas restoring *Shank3* expression specifically in CoA pyramidal neurons reversed these structural, physiological, and behavioral abnormalities. These findings establish a causal role for Shank3 expression in CoA neurons in facilitating adaptive interactions with chemical—and potentially social—environment in mice, presenting opportunities for diagnostic and therapeutic intervention.

Human and animal studies demonstrate that the amygdala plays a central role in valence coding, driving both innate and learned behavioral responses, with distinct functional contributions from its subnuclei. The basolateral amygdala (BLA) and central amygdala (CeA) are critical for learned appetitive and aversive behaviors elicited by CS (*17*, *37*–*39*). For innate behaviors, however, lesion studies indicate that the BLA and CeA are dispensable for predator odor-induced aversion in mice. In contrast, the CoA and medial amygdala (MeA) regulate predator odor-evoked avoidance, whereas the CoA is also essential for processing attractive odor cues (*19*, *40*, *41*). In this study, selective deletion of Shank3 in the CoA using CRISPR-Cas9 recapitulates the olfactory valence deficits observed in global *Shank3* KO mice, whereas selective restoration of Shank3 expression in the CoA rescues these deficits in global Shank3 KO mice. These findings provide compelling evidence that Shank3 expression in the CoA is essential for mediating odor valence–related behaviors. Our findings identify Shank3 as a critical molecular determinant whose loss in the CoA disrupts olfactory valence processing, providing a mechanistic link between *SHANK3* deficiency and sensory abnormalities relevant to ASD.

The *Shank3* gene is broadly expressed across both nonlimbic and limbic brain structures, exhibiting regional differences in expression levels and functional roles, and modulating neural activity within distinct circuits. Loss of *Shank3* in nonlimbic brain regions, including the motor cortex (M1), somatosensory cortex (S1), barrier cortex, prefrontal cortex (PFC), and dorsal striatum, leads to aberrant cortical and subcortical connectivity, contributing to the core motor, sensory, and cognitive impairments characteristic of ASD (*42*–*46*). The role of *Shank3* expression in the limbic system is less well understood but has been associated with reward processing, emotional regulation, memory, and social behavior (*47*, *48*). For instance, *Shank3* is highly expressed in the anterior cingulate cortex (ACC), where its dysfunction results in deficits in social interactions, driven by impaired excitatory synaptic transmission and neural circuit connectivity (*49*). In the PIR, *Shank3* is crucial for target odor recognition, with its haploinsufficiency selectively impairing the ability to discriminate target odors within unfamiliar olfactory backgrounds (*50*). Although *Shank3* expression in the CoA is relatively low compared to other limbic and nonlimbic structures (*42*), we observed marked hypoactivity in CoA neurons of *Shank3* mutant mice, attributable to reduced excitatory synaptic transmission and dendritic spine abnormalities. The phenotypic differences of mEPSC amplitude phenotype (*Shank3B* KO mice, $sgRNA^{Shank3}$ mice, and *Shank3* CKI mice) likely stem from the timing and cellular specificity of the Shank3 deletion. The chronic, germline *Shank3* knockout leads to a homogeneous, complete loss of *Shank3*, whereas the acute, AAV-*SpCas9-sgRNA*-mediated deletion in adults likely results in an incomplete knockout efficiency within the CoA cell population. The conditional rescue model (CKI) uses a yet distinct genetic strategy to delete most major *Shank3* isoforms. These three distinct methodological distinctions were associated with decreased mEPSC frequency, and changes in CoA pyramidal neuron morphology and spine density were observed in two Shank3 mutant models. This observation sheds light on how *Shank3* mutations impair olfactory-driven emotional responses, further elucidating its role in the limbic system and sensory-affective integration.

We note that the CoA mechanisms identified in mice cannot be directly extended to humans. A recent human magnetic resonance imaging (MRI) study has linked *SHANK3* defects with reduced amygdala gray matter volume (*51*), but the spatial resolution of MRI does not allow clear characterization of CoA involvement. We also acknowledge that our findings are based on a small set of odors with distinct valence values. Nonetheless, *SHANK3* is one of the most well-established genetic factors associated with ASD (*3*, *52*) and core ASD phenotypes, including impairments in social behavior and sensory processing, are consistently observed in both individuals and animal models with *SHANK3* mutations (*53*). Distorted perception of social chemosignals has emerged as a contributor to socio-emotional difficulties in ASD (*54*). Given the intricate relationship between olfaction, emotion, and social function, our mouse findings highlight the potential of restoring *Shank3* expression in the CoA to rehabilitate odor valence processing and, ultimately, improve socio-emotional functions. Although these results motivate future investigation of amygdala-level mechanisms in individuals with *SHANK3* mutations and ASD, any therapeutic implications will require direct validation in clinical studies.

MATERIALS AND METHODS

Human participants

A total of 99 children, accompanied by their caregivers, participated in the human testing experiment. Of these, 22 participants (8 *SHANK3* and 14 TD children) were excluded due to data quality issues. Consequently, the data of 77 participants were included in the final analysis. For the nasal airflow assessment, the sample comprised 21 children with *SHANK3* deficiency (9 girls and 12 boys, 6.32 ± 2.09 years) and 42 age- and sex-matched TD children (18 girls and 24 boys, 6.36 ± 1.98 years). For the scalp EEG assessment, seven children with SHANK3 deficiency (three girls and four boys, 6.52 ± 1.98 years) and seven age- and sex-matched TD children (three girls and four boys, 6.64 ± 2.06 years) were included. *SHANK3* and TD groups did not differ in sex or age (nasal airflow: $\chi^2 = 0$, $P = 1$, $t_{61} = -0.07$, and $P = 0.94$; EEG: $\chi^2 = 0$, $P = 1$, $t_{12} = -0.11$, and $P = 0.91$). *SHANK3* mutations were identified through genetic testing, and gene reports were provided by caregivers. Demographic information and mutation details for the *SHANK3* group are summarized in table S1. None of the participants had respiratory allergies or upper respiratory infections at the time of testing. Written informed consent was obtained from the primary caregiver of each child to participate in the procedure, which was approved by the Institutional Review Boards at the Institute of Psychology (H22108) and the Shenzhen Institute of Advanced Technology (SIAT-IRB-220215-1-1-0587) of the Chinese Academy of Sciences.

Animals

All animal experiments were performed in accordance with the Shenzhen Institute of Advanced Technology (SIAT), Chinese Academy of Sciences guidelines for animal care and were approved by SIAT's Institutional Animal Care and Use Committee (IACUC, SIAT-IRB-180129-NS-HY-A0398). Animals were maintained on a 12-hour: 12-hour light:dark cycle (lights on at 08:00) with food and water provided ad libitum. Genotyping of *Shank3B* mice (the Jackson Laboratory, 017688) and *Shank3* CKI mice (a gift from W. Wang) was performed following standard protocols. We also used C57BL/6J mice (aged 6 to 8 weeks; Beijing Vital River Laboratory Animal Technology Co. Ltd.) in selective deletion of *Shank3* experiments. Our reported sample sizes in each experiment are comparable to those found in previous publications. Animals were randomly allocated to either a $sgRNA^{Shank3}$ or a $sgRNA^{Scr}$ group. Experimenters were blind to the experimental groups, and the order of testing was counterbalanced during behavioral experiments. No data were excluded from the analyses.

Olfactory stimuli

For human nasal airflow assessment, olfactory stimuli consisted of two pleasant fragrant oils—pineapple [50% (v/v) in propylene glycol] and chocolate [33% (v/v) in light mineral oil]—and two unpleasant odor compounds—trimethylamine [1% (v/v) in propylene glycol] and isovaleric acid [2% (v/v) in propylene glycol]. Trimethylamine has a rotten fishlike odor, whereas isovaleric acid has a sour stinky footlike odor. Each odor was presented using a felt-tip pen filled with 3 ml of the corresponding odor solution. For presentation, the cap was removed and the pen tip was positioned ~2 cm in front of both nostrils. For scalp EEG recordings, pineapple [5 and 0.5% (v/v) in propylene glycol] and trimethylamine [0.1 and 0.01% (v/v) in propylene glycol] at two concentration levels (1× and 0.1×) served as the olfactory stimuli, with purified air included as a control condition. Odors were delivered via a computer-controlled olfactometer providing a constant airflow of 2.5 liter/min.

The olfactory stimuli used for the Olfactory Valence Test comprised a panel of 11 odors that span diverse chemical categories and innate valence properties, including TMT, pentanal, furfural, 2-hexanone, propylene glycol (vehicle control), agmatine sulfate (AST), benzaldehyde, 2,3-butanedione, hexanal, IAA, and 2-PE. All odorants were prepared at a final concentration of 85 μmol/ml and dissolved in propylene glycol. For each trial, 50 μl of the odor solution was applied to a piece of filter paper and placed in a designated corner of the arena. The olfactory stimuli were presented for subsequent mechanistic behavioral experiments; we focused on two representative odorants—2-PE (appetitive) and TMT (aversive) [2-PE at 1% (v/v) in water, and the aversive odor, TMT, at a concentration of 300 μmol/ml in water]. During the testing phase, a 50-μl aliquot of each odor solution was applied to a piece of filter paper and placed in a designated corner of the experimental arena (*19*).

Human testing procedures

Nasal airflow assessment

Participants wore headphones and watched their favorite animated shows for ~20 min using GOOVIS G2 OLED display goggles mounted on a stand holder. Their eyes were positioned close to the micro-OLED displays. Concurrently, nasal flow was continuously measured using either a nasal cannula connected to a spirometer (FE141, AD Instruments) or a respiratory belt transducer (TN1132/ST, AD Instruments). The latter was used for two children with *SHANK3* who refused to wear a nasal cannula. The signals were amplified and recorded using a data acquisition device (Power Lab, AD Instruments) at a sampling rate of 1000 Hz. As depicted in Fig. 1A, the olfactory stimuli were intermittently presented in random order while the participants watched the animated shows. The odor pens were kept out of the participants' sight. Each odor was presented five to seven times, depending on the compliance of the participant. Each presentation lasted for 7 s, with a minimum interval of 25 s between consecutive odor presentations. There was no difference in the number of presentations between pleasant and unpleasant odors [$F(1,61) = 0.45$, $P = 0.51$].

In a separate task, TD children provided subjective valence ratings for each olfactory stimulus on a five-point scale marked by cartoon faces with sad (indicating unpleasant), somewhat sad, neutral, somewhat happy, and happy (pleasant) expressions. Both pineapple and chocolate were rated more pleasant than trimethylamine and isovaleric acid in TD children (fig. S1).

EEG recording

Participants watched their preferred animated shows on a 24-inch LED monitor for ~50 to 70 min. Olfactory stimuli were delivered via an olfactometer, with airflow held constant throughout testing. Each odor was presented 16 times, and the air control was presented 32 times, all in random order. Each presentation lasted 3 s, with an interstimulus interval of 17.5 to 18 s. The animated show was programmed to pause and display a fixed frame with no audio 0.5 to 1 s before each odor/air presentation, and this frame remained on the screen until the odor/air presentation ended. This procedure ensured consistent airflow and audiovisual input across olfactory conditions. Inhalation onsets were continuously monitored using a nasal pressure sensor (Sniff Logic; sampling rate: 200 Hz). Participants were allowed to discontinue the experiment at any point.

EEG data were continuously recorded from 32 Ag/AgCl scalp electrodes arranged according to the international 10-20 system (eego mylab, ANT Neuro). A 10% saline solution served as the conductive medium. Signals were referenced online to CPz and sampled at 500 Hz, and electrode impedance was maintained below 20 KΩ.

Stereotaxic virus injections

Mice (6 to 8 weeks of age) were anesthetized using chloral hydrate (1%, w/v) and positioned in a stereotaxic injection frame (RWD Life Science). A digital mouse brain atlas was linked to the injection frame to guide the identification and targeting of the CoA or the PIR. Injections were performed at a rate of 20 to 30 nl/min with a Hamilton syringe (10 μl, model 1701) using a Nanoliter 2000 microinjection system (WPI). Stereotaxic coordinates were used to direct injections into either the CoA [anteroposterior (AP), −1.40 mm; mediolateral (ML), −2.70 mm; and dorsoventral (DV), −5.80 mm) or the PIR (AP, −1.10 mm; ML, −3.70 mm; and DV, −4.70 mm]. To prevent backflow of fluid, the pipette was left in the brain for at least 5 min after completion of the injection. Once the injection pipette was removed, the mouse was removed from the stereotaxic apparatus, and the incision was closed with wound clips. During all surgical procedures, mice were kept on a heating pad and brought back to their home cages after recovery of movement.

We followed a published protocol for fiber photometry (*55*). Briefly, male mice were unilaterally injected with 300 nl of AAV9-*CaMKII*α-*GCaMP6s* (2.71×10^{12} vector genomes/ml), followed by the insertion of a ceramic cannula housing an optical fiber [1.25 mm in outer diameter (OD); 0.37 numerical aperture (NA)] toward the CoA or PIR. The ceramic cannula was then fixed with dental acrylic. Mice were individually housed for 2 weeks to allow GCaMP expression.

For sparse labeling (*56*), mice were injected with 100-nl mixtures of AAV9-*CaMKII*α-*Cre* (1:10,000) and AAV9-*EF1*α-*DIO-EGFP* for *Shank3B* mice or AAV9-*CaMKII*α-*FLP* (1:10,000) and AAV9-*EF1*α-*fDIO-mCherry* for *Shank3* CKI mice with methods mentioned above. Mice were brought back to their home cages for 3 weeks to allow reporter expression.

For selective deletion, 500 nl of AAV9-*pCALM1-SpCas9-miniU6-sgRNA*^{Shank3} or AAV9-*pCALM1-SpCas9-miniU6-sgRNA*^{Scr} (5×10^{12} vg/ml) was bilaterally injected into the CoA of C57BL/6J. Mice were brought back to their home cages for 4 weeks to ensure enough time for *Shank3* deletion.

For conditional knockout and rescue experiments, 500 nl of AAV8-*CaMKII*α-*Cre-EYFP* or AAV8-*CaMKII*α-*EYFP* (5×10^{12} vg/ml) was bilaterally injected into the CoA. Mice were brought back to their home cages for 3 weeks to allow Shank3 reexpression.

Replication was confirmed across different batches of animals and viral preparations.

Fiber photometry

A fiber photometry system (Thinker Tech) was used to record GCaMP signals in neurons. To record fluorescence signals, a 488-nm laser beam was reflected by a dichroic mirror, focused by a 10× objective lens, and then coupled to an optical commutator. An optical fiber (OD, 125 μm; NA = 0.37, 5.5/5 m long) guided the light between the commutator and the implanted optical fiber. The laser power was adjusted at the tip of the optical fiber to a low level of 0.01 to 0.02 mW to minimize bleaching. The GCaMP fluorescence was band-pass filtered (MF525-39, Thorlabs) and collected by a photomultiplier tube (R3896, Hamamatsu). An amplifier (C7319; Hamamatsu) was used to convert the photomultiplier tube current output to voltage signals, which was further filtered through a low-pass filter (40-Hz cutoff, Brownlee 440, AutoMate Scientific). The analog voltage signals were digitalized at 500 Hz and recorded by a Power 1401 digitizer and Spike2 software (CED) (*55*).

Head-fixed mice with optical fibers were connected to the fiber photometry system for recording. Responses were recorded following stimulation of 2-PE, TMT, or air presented for 3 s for each trial. Fiber photometry data were analyzed using MATLAB (MathWorks). The fluorescence change ($\Delta F/F$) was calculated as $(F - F_0)/F_0$, where F_0 was the mean fluorescence signal during a 1-s baseline period in each trial. The area under the curve (AUC) was calculated as mean $\Delta F/F$ during a 10-s period (0 to 10 s from onset).

Olfactory Valence Test

The olfactory preference test was conducted with modifications from a previously established protocol (*19*, *57*). Before each behavioral session, mice were transferred to a dedicated testing room and allowed to acclimate for at least 30 min. Adult male mice were tested individually in a 40 cm–by–40 cm–by–45 cm (width × length × height) open-field arena. At the beginning of each trial, a clean piece of filter paper (1.5 cm by 2 cm) was placed in the designated target quadrant and remained there throughout the entire 15-min session.

Mice were first allowed to freely explore the arena for 5 min without odor stimulation. This odor-free period was used to quantify each mouse's baseline preference for the target quadrant. Immediately after the baseline phase, 50 μl of the odorant solution (85 μmol/ml in propylene glycol) was gently applied to the filter paper without disturbing the animal, and the mouse continued exploring the arena for an additional 10 min. All sessions were video recorded, and the time spent in the target quadrant was analyzed using EthoVision XT.

For each mouse, the PI obtained under the solvent-alone condition (propylene glycol) was used as the individualized baseline. PI values obtained during odor stimulation were then normalized to this solvent PI, such that positive values reflected attraction and negative values reflected aversion relative to the solvent control.

Behavioral assay

Behavioral assays were performed in a 40 cm–by–40 cm–by–45 cm open-field chamber. A piece of filter paper (1.5 cm by 2 cm) was fixed in the target quadrant for the entire 15-min session. During the first 5 min (baseline period), no odorant was applied; during the subsequent 10 min (test period), 50 μl of the odorant solution (odorant diluted in water) was gently added to the filter paper without disturbing the animal. Water alone served as the vehicle control, and all performance indices were normalized to the vehicle baseline (*58*). All odorant exposures were performed in thoroughly cleaned chambers, with 75% ethanol used between trials to eliminate residual olfactory cues.

Behavioral videos were recorded and analyzed using EthoVision XT (Noldus). The investigation time was defined as the cumulative duration during which the mouse's nose entered the predefined filter paper region of interest (ROI). Maximum velocity was calculated as the peak instantaneous speed within the target quadrant during odor exposure. Immobility time was quantified using EthoVision's standard mobility thresholds, defined as episodes in which whole-body movement fell within 0.05 to 60% of the activity detection threshold for at least 2 s. Total distance traveled was extracted as an

index of general locomotor activity and used to rule out nonspecific motor deficits.

Odor-reward associative learning

Mice were water deprived for 48 hours and habituated to a head-fixed setup. Odor delivery, water reward, and lick detection were controlled by an Arduino-based system interfaced with MATLAB. During Pavlovian conditioning, a 1-s odor stimulus (CS) preceded water delivery (US) by 2 s. Anticipatory licking was quantified during a 2-s response window before reward delivery. The intertrial interval was randomized between 6 and 8 s. Mice received ~40 trials per session per day, and behavior was analyzed offline in MATLAB. Well-trained mice (three to six sessions) exhibited robust anticipatory licking (≥80% of maximal lick rate) following odor presentation.

Electrophysiology

Whole-cell patch-clamp recording was performed as described previously (*59*, *60*). Briefly, the mice were anesthetized with isoflurane and brains were removed and placed in ice-cold dissection solution saturated with 95% O_2 and 5% CO_2 containing the following: 115 mM NaCl, 2.5 mM KCl, 1.25 mM NaH_2PO_4, 0.1 mM $CaCl_2$, 3 mM $MgCl_2$, 25 mM $NaHCO_3$, 25 mM glucose, 0.4 mM L-ascorbic acid, 3 mM myo-inositol, and 2 mM sodium pyruvate. Coronal slices (300 μm) containing the CoA region were prepared using a vibratome (VT1200S, Leica). Slices were then transferred to a recovery chamber containing the following: 115 mM NaCl, 2.5 mM KCl, 1.25 mM NaH_2PO_4, 2 mM $CaCl_2$, 1 mM $MgCl_2$, 25 mM $NaHCO_3$, 25 mM glucose, 0.4 mM L-ascorbic acid, 3 mM myo-inositol, and 2 mM sodium pyruvate (saturated with 95% O_2 and 5% CO_2, pH 7.4), for 30 min at 32°C and >30 min at room temperature before recording. Recordings were performed with internal solutions for recording excitatory synaptic responses, containing the following: 125 mM Cs-Meth, 20 mM CsCl, 5 mM Na_2Phosphocreatine, 4 mM MgATP, 0.3 mM NaGTP, 0.5 mM EGTA, and 2 mM QX-314 (pH 7.3). Patch pipettes were pulled from borosilicate glass capillary tubes using a PC-100 pipette puller (Narishige). The resistance of pipettes filled with intracellular solution varied between 4 and 5 MΩ.

The recordings were obtained using a Multiclamp 700B amplifier (Molecular Devices). For all whole-cell recordings, membrane resistance was monitored before and after each run. Cells were rejected if Ra was >30 MΩ and leaky current >500 pA throughout the experiment. Recordings were digitized and filtered with a Digidata 1550B. Clampex 10.7 was used for acquisition and analysis. Experimenters were unaware of the genotype of all samples throughout data collection and analysis.

For the recording of PPR and AMPAR-mediated input-output curve, the cells were voltage clamped at −70 mV in the presence of 50 μM D-AP5 to block NMDA receptors (NMDARs) and 50 μM picrotoxin to block inhibitory synaptic transmission. The evoked AMPAR-mediated synaptic responses were triggered by a bipolar electrode placed in Layer I (100 to 150 μm from the soma of neurons recorded). The paired stimuli were delivered at an interstimulus interval of 50 ms. The PPR is calculated by the ratio of the peak response of the second EPSC to that of the first EPSC. For the AMPA-to-NMDA ratio, the AMPAR- and NMDAR-mediated EPSCs were recorded in the presence of 50 μM picrotoxin at holding membrane potentials of −70 and +40 mV, respectively. The AMPA-to-NMDA ratio was calculated as the ratio of the average AMPA-EPSC peak amplitude to the NMDA-EPSC amplitude. For the recording of mEPSCs, the cells were voltage clamped at −70 mV in the presence of 50 μM picrotoxin to block $GABA_A$ (γ-aminobutyric acid type A) receptors and 1 μM TTX to block action potentials. The mEPSCs were digitized at 20 kHz, filtered at 2 kHz, and analyzed with Mini Analysis (Synaptosoft Inc.).

Immunofluorescence and imaging

Mice were anesthetized with chloral hydrate (1%, w/v) and perfused transcardially with cold phosphate-buffered saline (PBS) and 4% paraformaldehyde (PFA) to remove blood. Thick coronal sections (40 μm) were collected throughout the whole brain. Following PBS washes, samples were blocked in BlockAid (B10710, Invitrogen) containing 0.3% (w/v) Triton X-100 for 1 hour at room temperature. Sections were overlaid with anti-c-Fos antibody (1:400, 9F6, Cell Signaling Technology), anti-HA antibody (1:400, C29F4, CST), or anti-GFP antibody (1:500, 600-301-215, Rockland) and incubated for 48 hours at 4°C. After washing off the primary antibody, samples were overlaid with a 1:500 dilution of Alexa Fluor 488 Goat-anti-Rabbit IgG (111-545-144, Jackson ImmunoResearch) or Alexa Fluor 488 Goat-anti-Mouse IgG (115-545-003, Jackson ImmunoResearch) and incubated at room temperature for 2 hours. After washing, sections were coverslipped with Fluoroshield mounting medium with 4′,6-diamidino-2-phenylindole (DAPI; ab104139, Abcam).

c-Fos–positive cells were quantified from anatomically matched coronal sections identified according to the Allen brain atlas. For each animal, two sections were collected from the OB (bregma: +4.2 to +3.8 mm), three from the CoA and the PIR (bregma: −1.2 to −2.4 mm), using evenly spaced 120-μm intervals to cover posteromedial (CoApm) and posterolateral (CoApl) subdivisions. For each mouse, the reported value represents the average c-Fos count across all sections for each region. Each group included three mice, and all individual animal data points are shown.

Images were acquired with an Axio Imager Z2 microscope (Zeiss) or an LSM 900 Confocal microscope (Zeiss). ROIs were defined using atlas-guided anatomical boundaries and verified by a blinded experimenter. c-Fos^+ nuclei were counted using consistent thresholding parameters in Imaris (Oxford Instruments). For each mouse, the reported value represents the average c-Fos count across the two/three sections for each region.

Real-time quantitative polymerase chain reaction

Total RNA was extracted using RNAiso Plus (9109, Takara) according to the manufacturer's instructions. cDNA was synthesized from total RNA using a reverse transcription kit (11155ES60, Yeasen). Quantitative polymerase chain reaction (qPCR) was subsequently performed using the SYBR Green Master Mix (311185ES03, Yeasen). All primers were synthesized by Tsingke Biotechnology (Shenzhen, China). The primer sequences were as follows: *Shank3*: forward 5′-CCTATGACAGCCTCACTTCACACAG-3′, reverse 5′-GACCCAC-CACTTGCTTGTGTCCAAC-3′; β-actin (internal control): forward 5′-AGTGTGACGTTGACATCCGT-3′, reverse 5′-TGCTAGGAGC-CAGAGCAGTA-3′.

For qPCR analysis, each biological sample (tissue from an individual mouse) was assayed in three technical replicates (triplicate wells). The mean of the three technical replicates was used as the value for each biological replicate for subsequent statistical analysis.

Western blotting analysis

CoA and PIR tissues were microdissected in ice-cold oxygenated ACSF (artificial cerebrospinal fluid) and lysed in RIPA (radioimmunoprecipitation assay) buffer (20115ES60, Yeasen) containing protease inhibitors. After centrifugation, protein concentrations were determined using a BCA assay (23235, Invitrogen). Equal amounts of protein were resolved by SDS–polyacrylamide gel electrophoresis and transferred to PVDF (polyvinylidene difluoride) membranes. Membranes were blocked with 5% nonfat milk and incubated overnight at 4°C with a primary antibody against Shank3 (1:1000, 64555S, CST) and Tubulin (1:5000, 66031, Proteintech), followed by HRP (horseradish peroxidase)–conjugated secondary antibody (1:1000, 7074P2, CST). Signals were detected using enhanced chemiluminescence and quantified in ImageJ. Shank3 expression was normalized to Tubulin for each lane.

For Western blot analyses, biological replicates consisted of protein lysates prepared from three independent mice per group, with each mouse contributing one sample to the analysis.

Analyses of human data

Nasal airflows

Nasal airflows were analyzed following established methods (*61*, *62*). The original respiratory signals were downsampled to 100 Hz and low-pass filtered at 10 Hz using FieldTrip (*63*). The onset and offset of each inhalation and exhalation were estimated using BreathMetrics (*64*) and were visually inspected to ensure accuracy. Within each 7-s odor presentation period, two nasal inhalations were identified (Sniff 1 followed by Sniff 2). To account for variations in respiratory signals across the recording session, each of Sniff 1 and Sniff 2 was normalized by respectively dividing the duration and flowrate by the baseline inhalation duration and peak inhalation flowrate, calculated as the averages of the three inhalations preceding the odor presentation. In addition, the following parameters were extracted for each sniff trace: mean sniff flowrate, peak sniff flowrate, sniff duration, and sniff volume, each similarly normalized by its respective baseline values. Trials without three stable baseline inhalations, two identifiable inhalations during the odor presentation period, or with sniff volumes exceeding 3.5 SDs from the mean were excluded from the analysis. Participants with fewer than four trials in any odor condition were excluded from group-level analysis to ensure data quality.

EEG data

EEG data were preprocessed using FieldTrip (*63*). After re-referencing to the common average and applying a 1- to 45-Hz zero-phase Butterworth band-pass filter, the continuous EEG recordings were segmented into 6-s epochs ranging from −2 to 4 s relative to odor/air delivery. Epochs containing substantial head movements, artifacts, or abnormalities noted in the experimental log were removed. Independent component analysis (ICA) was then performed to identify and remove ocular artifacts from the remaining data.

Time-frequency decomposition of single-trial epochs was conducted using continuous Morlet wavelet convolution. Morlet wavelets with a fixed width of four cycles were constructed for frequencies from 2 to 15 Hz in 0.5-Hz steps. Each trial was subsequently re-epoched by aligning to the first inhalation onset following odor/air delivery. Time-frequency data were baseline normalized to the −500 to −200 ms prestimulus interval, computed as: $ER\%_{t,f} = (A_{t,f} - B_f)/B_f$, where $A_{t,f}$ is the power at latency t and frequency f, and B_f is the mean baseline power at frequency f.

Quantification and statistical analysis

All experiments were conducted blinded, including the electrophysiology and behavioral analyses. The number of replicates (n) is indicated in the figure legends and refers to the number of experimental subjects independently treated in each experimental condition. Statistical analyses were performed in SPSS (version 22, IBM), JASP (2023, version 0.17), and GraphPad (version 9, Prism). Sniff response differences between means in the pleasant and unpleasant odorant conditions were compared against zero using one-sample Student's t tests. The modulation differences between means across TD and *SHANK3* groups were tested for statistical significance using the two-tailed unpaired t test. Additional Bayesian independent samples t tests were conducted to compare the sniff response differences between subgroups of children with *SHANK3*. The sex ratio between groups was assessed by the chi-square test. Normally distributed data were tested by one-way ANOVA followed by Dunnett's test or Tukey's test for multiple comparisons and unpaired two-sample Student's t test for two-group comparisons. Probabilities of $P < 0.05$ were considered to be statistically significant.

Supplementary Materials

This PDF file includes:

Figs. S1 to S12
Table S1

REFERENCES

1. J. L. Costales, A. Kolevzon, Phelan-McDermid syndrome and SHANK3: Implications for treatment. *Neurotherapeutics* **12**, 620–630 (2015).
2. D. M. Cochoy, A. Kolevzon, Y. Kajiwara, M. Schoen, M. Pascual-Lucas, S. Lurie, J. D. Buxbaum, T. M. Boeckers, M. J. Schmeisser, Phenotypic and functional analysis of SHANK3 stop mutations identified in individuals with ASD and/or ID. *Mol. Autism* **6**, 23 (2015).
3. P. Monteiro, G. Feng, SHANK proteins: Roles at the synapse and in autism spectrum disorder. *Nat. Rev. Neurosci.* **18**, 147–157 (2017).
4. M. B. First, Diagnostic and statistical manual of mental disorders, 5th edition, and clinical utility. *J. Nerv. Ment. Dis.* **201**, 727–729 (2013).
5. T. Tavassoli, C. Layton, T. Levy, M. Rowe, J. George-Jones, J. Zweifach, S. Lurie, J. D. Buxbaum, A. Kolevzon, P. M. Siper, Sensory reactivity phenotype in Phelan-McDermid syndrome is distinct from idiopathic ASD. *Genes (Basel)* **12**, 977 (2021).
6. L. B. Buck, C. Bargmann, "Smell and taste: The chemical senses" in *Principles of Neural Science, Fifth Edition* (McGraw-Hill Education, New York, NY, 2014).
7. R. I. Wilson, Z. F. Mainen, Early events in olfactory processing. *Annu. Rev. Neurosci.* **29**, 163–201 (2006).
8. D. L. Sosulski, M. L. Bloom, T. Cutforth, R. Axel, S. R. Datta, Distinct representations of olfactory information in different cortical centres. *Nature* **472**, 213–216 (2011).
9. Y. Li, J. Xu, Y. Liu, J. Zhu, N. Liu, W. Zeng, N. Huang, M. J. Rasch, H. Jiang, X. Gu, X. Li, M. Luo, C. Li, J. Teng, J. Chen, S. Zeng, L. Lin, X. Zhang, A distinct entorhinal cortex to hippocampal CA1 direct circuit for olfactory associative learning. *Nat. Neurosci.* **20**, 559–570 (2017).
10. S. Boesveldt, V. Parma, The importance of the olfactory system in human well-being, through nutrition and social behavior. *Cell Tissue Res.* **383**, 559–567 (2021).
11. K. Asahina, V. Pavlenkovich, L. B. Vosshall, The survival advantage of olfaction in a competitive environment. *Curr. Biol.* **18**, 1153–1155 (2008).
12. D. P. Devanand, S. Lee, J. Manly, H. Andrews, N. Schupf, A. Masurkar, Y. Stern, R. Mayeux, R. L. Doty, Olfactory identification deficits and increased mortality in the community. *Ann. Neurol.* **78**, 401–411 (2015).
13. J. A. Russell, A circumplex model of affect. *J. Pers. Soc. Psychol.* **39**, 1161–1178 (1980).
14. R. Haddad, H. Lapid, D. Harel, N. Sobel, Measuring smells. *Curr. Opin. Neurobiol.* **18**, 438–444 (2008).
15. R. Krieglmeyer, R. Deutsch, J. De Houwer, R. De Raedt, Being moved: Valence activates approach-avoidance behavior independently of evaluation and approach-avoidance intentions. *Psychol. Sci.* **21**, 607–613 (2010).
16. J. S. Winston, J. A. Gottfried, J. M. Kilner, R. J. Dolan, Integrated neural representations of odor intensity and affective valence in human amygdala. *J. Neurosci.* **25**, 8903–8907 (2005).

17. M. Pignatelli, A. Beyeler, Valence coding in amygdala circuits. *Curr. Opin. Behav. Sci.* **26**, 97–106 (2019).
18. X. Zhang, W. Guan, T. Yang, A. Furlan, X. Xiao, K. Yu, X. An, W. Galbavy, C. Ramakrishnan, K. Deisseroth, K. Ritola, A. Hantman, M. He, Z. Josh Huang, B. Li, Genetically identified amygdala-striatal circuits for valence-specific behaviors. *Nat. Neurosci.* **24**, 1586–1600 (2021).
19. C. M. Root, C. A. Denny, R. Hen, R. Axel, The participation of cortical amygdala in innate, odour-driven behaviour. *Nature* **515**, 269–273 (2014).
20. S. Baron-Cohen, H. A. Ring, E. T. Bullmore, S. Wheelwright, C. Ashwin, S. C. Williams, The amygdala theory of autism. *Neurosci. Biobehav. Rev.* **24**, 355–364 (2000).
21. A. Tseng, R. Bansal, J. Liu, A. J. Gerber, S. Goh, J. Posner, T. Colibazzi, M. Algermissen, I. C. Chiang, J. A. Russell, B. S. Peterson, Using the circumplex model of affect to study valence and arousal ratings of emotional faces by children and adults with autism spectrum disorders. *J. Autism Dev. Disord.* **44**, 1332–1346 (2014).
22. I. Perini, P. A. Gustafsson, K. Igelstrom, B. Jasiunaite-Jokubaviciene, R. Kampe, L. M. Mayo, J. Molander, H. Olausson, M. Zetterqvist, M. Heilig, Altered relationship between subjective perception and central representation of touch hedonics in adolescents with autism-spectrum disorder. *Transl. Psychiatry* **11**, 224 (2021).
23. S. J. Palmer, A. Fanucci-Kiss, E. Kipervassar, I. Jalnapurkar, S. M. Hodge, J. A. Frazier, D. Cochran, Effect of emotional valence on emotion recognition in adolescents with autism spectrum disorder. *J. Autism Dev. Disord.* **54**, 1494–1506 (2024).
24. A. V. Aubry, R. Durand-de Cuttoli, E. Karpman, R. L. Fisher-Foye, L. F. Parise, F. Cathomas, C. J. Burnett, Y. Yang, C. Yuan, A. R. LaBanca, K. L. Chan, K. T. Winston, H. Y. Lin, F. Dackour, A. A. Tavallaei, J. Alvarez, T. Nishioka, H. Morishita, R. C. Froemke, L. Li, S. J. Russo, A crucial role for the cortical amygdala in shaping social encounters. *Nature* **639**, 1006–1015 (2025).
25. S. De Rubeis, P. M. Siper, A. Durkin, J. Weissman, F. Muratet, D. Halpern, M. D. P. Trelles, Y. Frank, R. Lozano, A. T. Wang, J. L. Holder Jr., C. Betancur, J. D. Buxbaum, A. Kolevzon, Delineation of the genetic and clinical spectrum of Phelan-McDermid syndrome caused by SHANK3 point mutations. *Mol. Autism* **9**, 31 (2018).
26. A. Vogels, G. Droogmans, E. Vergaelen, G. Van Buggenhout, A. Swillen, Recent developments in Phelan-McDermid syndrome research: An update on cognitive development, communication and psychiatric disorders. *Curr. Opin. Psychiatry* **34**, 118–122 (2021).
27. G. Kobal, T. Hummel, S. Vantoller, Differences in human chemosensory evoked-potentials to olfactory and somatosensory chemical stimuli presented to left and right nostrils. *Chem. Sens.* **17**, 233–244 (1992).
28. A. M. Lascano, T. Hummel, J. S. Lacroix, B. N. Landis, C. M. Michel, Spatio-temporal dynamics of olfactory processing in the human brain: An event-related source imaging study. *Neuroscience* **167**, 700–708 (2010).
29. W. R. Klemm, S. D. Lutes, D. V. Hendrix, S. Warrenburg, Topographical EEG maps of human responses to odors. *Chem. Sens.* **17**, 347–361 (1992).
30. T. S. Lorig, G. E. Schwartz, Brain and odor: I. Alteration of human EEG by odor administration. *Psychobiology* **16**, 281–284 (1988).
31. M. Kato, T. Okumura, K. Touhara, M. Okamoto, Behavioral relevance of early neural coding of low-level odor features in humans. *J. Neurosci.* **45**, e0203252025 (2025).
32. K. Kondoh, Z. Lu, X. Ye, D. P. Olson, B. B. Lowell, L. B. Buck, A specific area of olfactory cortex involved in stress hormone responses to predator odours. *Nature* **532**, 103–106 (2016).
33. L. Tian, S. A. Hires, L. L. Looger, Imaging neuronal activity with genetically encoded calcium indicators. *Cold Spring Harb. Protoc.* **2012**, 647–656 (2012).
34. Y. Mei, P. Monteiro, Y. Zhou, J. A. Kim, X. Gao, Z. Fu, G. Feng, Adult restoration of Shank3 expression rescues selective autistic-like phenotypes. *Nature* **530**, 481–484 (2016).
35. Y. Yeshurun, N. Sobel, An odor is not worth a thousand words: From multidimensional odors to unidimensional odor objects. *Annu. Rev. Psychol.* **61**, 219–241, C211–C215 (2010).
36. N. H. Frijda, B. Mesquita, "The social roles and functions of emotions" in *Emotion and Culture: Empirical Studies of Mutual Influence*, S. Kitayama, H. R. Markus, Eds. (American Psychological Association, 1994), pp. 51–87.
37. M. S. Kehl, S. Mackay, K. Ohla, M. Schneider, V. Borger, R. Surges, M. Spehr, F. Mormann, Single-neuron representations of odours in the human brain. *Nature* **634**, 626–634 (2024).
38. A. Govic, A. G. Paolini, In vivo electrophysiological recordings in amygdala subnuclei reveal selective and distinct responses to a behaviorally identified predator odor. *J. Neurophysiol.* **113**, 1423–1436 (2015).
39. T. Isosaka, T. Matsuo, T. Yamaguchi, K. Funabiki, S. Nakanishi, R. Kobayakawa, K. Kobayakawa, Htr2a-expressing cells in the central amygdala control the hierarchy between innate and learned fear. *Cell* **163**, 1153–1164 (2015).
40. H. Wang, Q. Wang, L. Cui, X. Feng, P. Dong, L. Tan, L. Lin, H. Lian, S. Cao, H. Huang, P. Cao, X. M. Li, A molecularly defined amygdala-independent tetra-synaptic forebrain-to-hindbrain pathway for odor-driven innate fear and anxiety. *Nat. Neurosci.* **27**, 514–526 (2024).
41. C. I. Li, T. L. Maglinao, L. K. Takahashi, Medial amygdala modulation of predator odor-induced unconditioned fear in the rat. *Behav. Neurosci.* **118**, 324–332 (2004).
42. J. Peça, C. Feliciano, J. T. Ting, W. Wang, M. F. Wells, T. N. Venkatraman, C. D. Lascola, Z. Fu, G. Feng, Shank3 mutant mice display autistic-like behaviours and striatal dysfunction. *Nature* **472**, 437–442 (2011).
43. Q. Chen, C. A. Deister, X. Gao, B. Guo, T. Lynn-Jones, N. Chen, M. F. Wells, R. Liu, M. J. Goard, J. Dimidschstein, S. Feng, Y. Shi, W. Liao, Z. Lu, G. Fishell, C. I. Moore, G. Feng, Dysfunction of cortical GABAergic neurons leads to sensory hyper-reactivity in a Shank3 mouse model of ASD. *Nat. Neurosci.* **23**, 520–532 (2020).
44. M. Pagani, A. Bertero, A. Liska, A. Galbusera, M. Sabbioni, N. Barsotti, N. Colenbier, D. Marinazzo, M. L. Scattoni, M. Pasqualetti, A. Gozzi, Deletion of autism risk gene Shank3 disrupts prefrontal connectivity. *J. Neurosci.* **39**, 5299–5310 (2019).
45. F. Zhu, Q. Shi, Y. H. Jiang, Y. Q. Zhang, H. Zhao, Impaired synaptic function and hyperexcitability of the pyramidal neurons in the prefrontal cortex of autism-associated Shank3 mutant dogs. *Mol. Autism* **15**, 9 (2024).
46. Q. Shi, L. Wu, B. Ren, K. Guo, Y. H. Jiang, Y. Q. Zhang, L. Hu, Impaired tactile processing in autism-associated Shank3 mutant dogs: Neural mechanism and intervention. *Sci. Bull.* **70**, 483–487 (2025).
47. S. Bariselli, S. Tzanoulinou, C. Glangetas, C. Prévost-Solié, L. Pucci, J. Viguié, P. Bezzi, E. C. O'Connor, F. Georges, C. Lüscher, C. Bellone, SHANK3 controls maturation of social reward circuits in the VTA. *Nat. Neurosci.* **19**, 926–934 (2016).
48. F. Raynaud, A. Janossy, J. Dahl, F. Bertaso, J. Perroy, A. Varrault, M. Vidal, P. F. Worley, T. M. Boeckers, J. Bockaert, P. Marin, L. Fagni, V. Homburger, Shank3-Rich2 interaction regulates AMPA receptor recycling and synaptic long-term potentiation. *J. Neurosci.* **33**, 9699–9715 (2013).
49. B. Guo, J. Chen, Q. Chen, K. Ren, D. Feng, H. Mao, H. Yao, J. Yang, H. Liu, Y. Liu, F. Jia, C. Qi, T. Lynn-Jones, H. Hu, Z. Fu, G. Feng, W. Wang, S. Wu, Anterior cingulate cortex dysfunction underlies social deficits in Shank3 mutant mice. *Nat. Neurosci.* **22**, 1223–1234 (2019).
50. D. Ryndych, A. Sebold, A. Strassburg, Y. Li, R. L. Ramos, G. H. Otazu, Haploinsufficiency of Shank3 in mice selectively impairs target odor recognition in novel background odors. *J. Neurosci.* **43**, 7799–7811 (2023).
51. C. Liu, D. Li, H. Yang, H. Li, Q. Xu, B. Zhou, C. Hu, C. Li, Y. Wang, Z. Qiao, Y. H. Jiang, X. Xu, Altered striatum centered brain structures in SHANK3 deficient Chinese children with genotype and phenotype profiling. *Prog. Neurobiol.* **200**, 101985 (2021).
52. H. Y. Zoghbi, M. F. Bear, Synaptic dysfunction in neurodevelopmental disorders associated with autism and intellectual disabilities. *Cold Spring Harb. Perspect. Biol.* **4**, a009886 (2012).
53. Y. Zhou, J. Sharma, Q. Ke, R. Landman, J. Yuan, H. Chen, D. S. Hayden, J. W. Fisher III, M. Jiang, W. Menegas, T. Aida, T. Yan, Y. Zou, D. Xu, S. Parmar, J. B. Hyman, A. Fanucci-Kiss, O. Meisner, D. Wang, Y. Huang, Y. Li, Y. Bai, W. Ji, X. Lai, W. Li, L. Huang, Z. Lu, L. Wang, S. A. Anteraper, M. Sur, H. Zhou, A. P. Xiang, R. Desimone, G. Feng, S. Yang, Atypical behaviour and connectivity in SHANK3-mutant macaques. *Nature* **570**, 326–331 (2019).
54. Y. Endevelt-Shapira, O. Perl, A. Ravia, D. Amir, A. Eisen, V. Bezalel, L. Rozenkrantz, E. Mishor, L. Pinchover, T. Soroka, D. Honigstein, N. Sobel, Altered responses to social chemosignals in autism spectrum disorder. *Nat. Neurosci.* **21**, 111–119 (2018).
55. Y. Li, W. Zhong, D. Wang, Q. Feng, Z. Liu, J. Zhou, C. Jia, F. Hu, J. Zeng, Q. Guo, Serotonin neurons in the dorsal raphe nucleus encode reward signals. *Nat. Commun.* **7**, 10503 (2016).
56. M. N. Economo, N. G. Clack, L. D. Lavis, C. R. Gerfen, K. Svoboda, E. W. Myers, J. Chandrashekar, A platform for brain-wide imaging and reconstruction of individual neurons. *Elife* **5**, e10566 (2016).
57. L. R. Saraiva, K. Kondoh, X. Ye, K. H. Yoon, M. Hernandez, L. B. Buck, Combinatorial effects of odorants on mouse behavior. *Proc. Natl. Acad. Sci. U.S.A.* **113**, E3300–E3306 (2016).
58. C. Henderson, L. Wijetunge, M. N. Kinoshita, M. Shumway, R. S. Hammond, F. R. Postma, C. Brynczka, R. Rush, A. Thomas, R. Paylor, S. T. Warren, P. W. Vanderklish, P. C. Kind, R. L. Carpenter, M. F. Bear, A. M. Healy, Reversal of disease-related pathologies in the fragile X mouse model by selective activation of GABAB receptors with arbaclofen. *Sci. Transl. Med.* **4**, 152ra128 (2012).
59. Y. Han, R. Cao, L. Qin, L. Y. Chen, A. H. Tang, T. C. Südhof, B. Zhang, Neuroligin-3 confines AMPA receptors into nanoclusters, thereby controlling synaptic strength at the calyx of Held synapses. *Sci. Adv.* **8**, eabo4173 (2022).
60. L. Qin, Z. Liu, S. Guo, Y. Han, X. Wang, W. Ren, J. Chen, H. Zhen, C. Nie, K. K. Xing, T. Chen, T. C. Südhof, Y. Sun, B. Zhang, Astrocytic Neuroligin-3 influences gene expression and social behavior, but is dispensable for synapse number. *Mol. Psychiatry* **30**, 84–96 (2025).
61. A. Arzi, L. Rozenkrantz, L. Gorodisky, D. Rozenkrantz, Y. Holtzman, A. Ravia, T. A. Bekinschtein, T. Galperin, B. Z. Krimchansky, G. Cohen, A. Oksamitni, E. Aidinoff, Y. Sacher, N. Sobel, Olfactory sniffing signals consciousness in unresponsive patients with brain injuries. *Nature* **581**, 428–433 (2020).
62. L. Rozenkrantz, D. Zachor, I. Heller, A. Plotkin, A. Weissbrod, K. Snitz, L. Secundo, N. Sobel, A mechanistic link between olfaction and autism spectrum disorder. *Curr. Biol.* **25**, 1904–1910 (2015).

63. R. Oostenveld, P. Fries, E. Maris, J. M. Schoffelen, FieldTrip: Open source software for advanced analysis of MEG, EEG, and invasive electrophysiological data. *Comput. Intell. Neurosci.* **2011**, 156869 (2011).
64. T. Noto, G. Zhou, S. Schuele, J. Templer, C. Zelano, Automated analysis of breathing waveforms using BreathMetrics: A respiratory signal processing toolbox. *Chem. Sens.* **43**, 583–597 (2018).

Acknowledgments: We thank C. Deng and members of the Lu laboratory for helpful discussions and comments. **Funding:** This work was supported by the Shenzhen Medical Research Fund grants B2402029 (Z.L.), B2302053 (Z.L.), and B2402228 (B.Z.); National Natural Science Foundation of China grants 31900715 (Y.H.), 32200865 (Y.W.), 82327805 (Z.L.), 82022018 (B.Z.), and 82161138025 (B.Z.); Ministry of Science and Technology of China grant STI2030-Major Projects 2021ZD0204200 (W.Z.); Strategic Priority Research Program of the Chinese Academy of Sciences grant XDB0930000 (Z.L.); Youth Team in Basic Research Field of Chinese Academy of Sciences grant YSBR-114 (Z.L.); Shenzhen Science and Technology Innovation Commission grant KQTD20210811090117032 (Z.L.); Shenzhen Technological Research Center for Primate Translational Medicine grant XMHT20220104005 (Z.L.); Shenzhen-Hong Kong Institute of Brain Science-Shenzhen Fundamental Research Institutions 2024SHIBS0004 (B.Z.); Guangdong Pearl River Funding (B.Z.); Major Program of Shenzhen Bay Laboratory 241101002 (B.Z.); Yunnan Technological Innovation Center of Drug Addiction Medicine 202305AK340001 (Y.Z.); and Brain Science and Brain-like Intelligence Technology–National Science and Technology Major Project 2021ZD0204200 (W.Z.). **Author contributions:** Methodology: Y.H., Y.W., M.W., G.C., and Y.Zh. Investigation: Y.H., Y.W., J.M., J.L., Q.L., J.Z., and R.W. Visualization: Y.H., Y.W., M.W., and G.C. Formal analysis: Y.H., Y.W., M.W., and Y.Zo. Supervision: Z.L., B.Z., W.Z., B.P., and Y.Zh. Writing—original draft: Y.H. and Y.W. Writing—review and editing: Z.L., B.Z., W.Z., and Q.C. **Competing interests:** The authors declare that they have no competing interests. **Data, code, and materials availability:** All data and code needed to evaluate and reproduce the results in the paper are present in the paper and/or the Supplementary Materials. Materials generated in this study are described in the Materials and Methods section.

Submitted 7 July 2025
Accepted 3 April 2026
Published 6 May 2026
10.1126/sciadv.aea3775

ScienceAdvances

SHANK3 mutations disrupt olfactory valence coding across species, with cortical amygdala mechanisms identified in mice

Yu Hu, Yuli Wu, Mingyu Wei, Jingchao Ma, Jianbang Lin, Gaowei Chen, Qi Li, Jianqing Zhang, Ruiqi Wang, Yingjie Zhu, Qian Chen, Bo Peng, Yingying Zou, Bo Zhang, Wen Zhou, and Zhonghua Lu

Sci. Adv. **12** (19), eaea3775. DOI: 10.1126/sciadv.aea3775